

1-1-2008

Magneto-acousto-electrical tomography : a potential imaging method for current density and electrical impedance

Syed Haider
Ryerson University

Follow this and additional works at: <http://digitalcommons.ryerson.ca/dissertations>



Part of the [Atomic, Molecular and Optical Physics Commons](#)

Recommended Citation

Haider, Syed, "Magneto-acousto-electrical tomography : a potential imaging method for current density and electrical impedance" (2008). *Theses and dissertations*. Paper 862.

This Thesis is brought to you for free and open access by Digital Commons @ Ryerson. It has been accepted for inclusion in Theses and dissertations by an authorized administrator of Digital Commons @ Ryerson. For more information, please contact bcameron@ryerson.ca.

RC
3826
T64
H35
2008

MAGNETO-ACOUSTO-ELECTRICAL TOMOGRAPHY: A POTENTIAL IMAGING METHOD FOR CURRENT DENSITY AND ELECTRICAL IMPEDANCE

By

Syed Haider

B.Eng., NED University, Pakistan, 2000

A thesis

presented to Ryerson University

in partial fulfillment of the

requirements for the degree of

Master of Science

in the Program of

Biomedical Physics

Toronto, Ontario, Canada, 2008

© Syed Haider, 2008

Author's Declaration

I hereby declare that I am the sole author of this thesis. I authorize Ryerson University to lend this thesis to other institutions or individuals for the purpose of scholarly research.

Syed Haider

I further authorize Ryerson University to reproduce this thesis by photocopying or by other means, in total or in part, at the request of other institutions or individuals for the purpose of scholarly research.

Syed Haider

MAGNETO-ACOUSTO-ELECTRICAL TOMOGRAPHY: A POTENTIAL IMAGING METHOD FOR CURRENT DENSITY AND ELECTRICAL IMPEDANCE

Syed Haider, B. Eng.

MSc Biomedical Physics, Ryerson University, Toronto, 2008

Abstract

This thesis is about investigating a potential imaging modality, magneto-acousto-electrical tomography (MAET), to provide high-spatial-resolution images of lead field current density and electrical impedance of biological tissues. A lead field current density distribution is the one obtained when a current/voltage source is applied to a sample via a pair of electrodes. The lead field current density distribution can potentially be used to obtain electrical impedance distribution which is helpful in differentiating normal and cancerous tissues. To image lead field current density, instead of directly applying a current/voltage source to the sample, the sample is placed in a static magnetic field and an ultrasound is focused on it to simulate a point like current dipole source in the focal zone. Electrodes are used to detect the voltage/current generated by the ultrasound in the sample, which according to the reciprocity theorem is proportional to a component of the lead field current density.

Acknowledgements

I am extremely grateful to Dr. Yuan Xu who gave me the opportunity to work under his supervision. He was always there to help me whenever I needed, whether it's about theory or experimental details. He graciously shared his knowledge, patience and time with me.

I would like to thanks Dr. Michael Kolios and Dr. Carl Kumaradas to be a part of my graduate committee. Dr. Kolios gave valuable suggestions during all the committee meetings and Dr. Kumaradas agreed to be an external examiner at the last moment.

Special thanks to my parents for their motivation and support. To my wife who initially opposed the idea of graduate studies but later fully supported it. She stood with me during difficult times and gave valuable suggestions. This achievement cannot be attained without her.

Finally I would also like to thank Arthur Worthington for his help during experiments, all faculty members, lab personnel and graduate students of Biomedical Physics for making my two years at Ryerson an unforgettable experience.

Table of Contents

Author's Declaration	ii
Abstract.....	iii
Acknowledgements	iv
Table of Contents	v
List of Tables	vii
List of Figures.....	viii
Chapter 1 Introduction.....	1
1.1 Electrical properties of a biological tissue	1
1.1.1 Charge carriers in a tissue.....	2
1.1.2 Cellular plasma membrane	2
1.1.3 Tissue dielectricity and conductivity	3
1.1.4 Frequency dependence of impedance.....	5
1.1.5 Equivalent circuit model of a biological cell.....	7
1.2 Electrical properties of a cancerous tissue	10
1.3 Electrical impedance of a tissue	10
1.4 Electrical impedance imaging	12
1.5 Hypothesis.....	14
1.6 Previous studies similar to MAET	15
1.7 Thesis contribution.....	16
Chapter 2 Theory	17
2.1 Reciprocity theorem	17
2.1.1 Discrete model	17
2.1.2 Continuous model.....	18
2.2 Derivation of the fundamental equation.....	19
Chapter 3 Experiment methods, Results and Discussions	24
3.1 Experimental setup and methods.....	24

3.2 Field profile of the transducers.....	25
3.2.1 Field profile of 1 MHz transducer.....	25
3.2.2 Field profile of 2.25 MHz transducer.....	27
3.3 Verification of MAET signals.....	28
3.3.1 MAET signal from a single point.....	29
3.3.2 MAET images.....	31
3.3.3 Cancellation of MAET signals in the interior of the sample.....	33
3.4 Imaging current density in a thin gel phantom sample with MAET.....	35
3.4.1 2D MAET image - experimental.....	35
3.4.2 2D MAET image - numerical simulation.....	38
3.4.3 Improvement of SNR by CHIRP.....	40
3.5 MAET images of biological tissues.....	44
3.5.1 2D MAET images.....	44
3.5.2 3D MAET images.....	48
Chapter 4 Challenges and Conclusions.....	54
4.1 Challenges and possible solutions.....	54
4.2 Summary.....	57
4.3 Conclusion.....	57
Bibliography.....	58

List of Tables

Table 3.1: Acoustic properties of oil and gel at 1 MHz.....	28
Table 3.2: Acoustic properties of oil and gel at 2.25MHz.....	36
Table 3.3: Acoustic properties of muscle and fat at 1 MHz.....	44

List of Figures

Figure 1.1: Biological cell and its constituents.....	1
Figure 1.2: The lipid bi-layer structure of the plasma membrane.....	2
Figure 1.3 (a): Schematics of a typical capacitor, (b): Equivalent circuit diagram	4
Figure 1.4: Frequency dependence of conductivity and permittivity in brain grey matter.....	6
Figure 1.5 (a): Equivalent electrical circuit of a cell, (b): Simplified model, (c): Simplified model after neglecting R_m	8
Figure 1.6: Paths of high and low frequency currents in a biological tissue	9
Figure 1.7: Volume conductor with specific impedance $z^*(\omega)$, length L , and cross-sectional area $S(x)$	11
Figure 1.8: Cylindrical conductor with resistivity ρ , length L , and cross-sectional area S , normal to the electric field \vec{E}	11
Figure 1.9: Illustration of lead field current density distribution in a sample.....	15
Figure 1.10: Schematics of MAET experimental setup.....	15
Figure 2.1: Reciprocity for discrete electrical circuit	18
Figure 2.2: Reciprocity for volume conductor.....	18
Figure 2.3: Generation of MAET signal in a thick block of gel phantom	22
Figure 3.1: Actual MAET experimental setup.....	25
Figure 3.2: 1 MHz transducer	26
Figure 3.3 (a): Field profile of 1 MHz transducer at the focus (b): Line plot along the dashed line	26
Figure 3.4: 2.25 MHz transducer	27
Figure 3.5 (a): Field profile of 2.25 MHz transducer at the focus (b): Line plot along the dashed line	27
Figure 3.6: Gel phantom with a rectangular cavity to verify MAET signal	28
Figure 3.7: MAET signal from two interfaces.....	29

Figure 3.8 (a): Perpendicular ultrasound incidence gives stronger signal (b): Angular ultrasound incidence gives weaker signal	30
Figure 3.9: MAET signal from four interfaces	31
Figure 3.10: Rectangular cavity phantom for MAET tomography.....	32
Figure 3.11: Tomographic MAET image of a rectangular cavity phantom	33
Figure 3.12: Schematics showing presence of MAET signal only at the interface of two mediums with different conductivities	34
Figure 3.13: Sample geometry for thin gel phantom	35
Figure 3.14: Image of J_{ab} from experiment. Lines l_1 and l_2 represents two scan levels	36
Figure 3.15: Line plots of J_{ab} in figure 3.14 along l_1 (dashed) and l_2 (solid).....	37
Figure 3.16: Image of J_{ab} from simulation. Lines l_1 and l_2 represents two scan levels	39
Figure 3.17: Line plots of J_{ab} in figure 3.16 along l_1 (dashed) and l_2 (solid).....	39
Figure 3.18: MAET signal obtained by sending a short pulse of 2 μ s.....	41
Figure 3.19: MAET signal obtained by sending a 1ms chirp pulse.....	42
Figure 3.20: Image of J_{ab} by a short pulse of 2 μ s	43
Figure 3.21: Image of J_{ab} by 1 ms chirp having a frequency sweep of 0.7-1.3 MHz.....	43
Figure 3.22: 2-layered biological sample.....	45
Figure 3.23: MAET tomography of a 2-layered biological sample.....	45
Figure 3.24: Electrodes for MAET experiments.....	46
Figure 3.25: 4-layered biological sample.....	47
Figure 3.26: MAET of a 4-layered biological sample	48
Figure 3.27: Biological sample for 3D MAET (a) top view (b) front view.....	49
Figure 3.28: Electrodes for 3D MAET	49
Figure 3.29: Tomographic images at cross-sections along y-axis	52
Figure 3.29: Tomographic images at cross-sections along y-axis	52

Chapter 1

Introduction

1.1 Electrical properties of a biological tissue

The biological tissue consists of cells and extra-cellular fluid. The constituents of a tissue determine its electrical properties. The cells occupy roughly 80% of the tissue volume and contain intra-cellular fluid inside a lipid membrane. The extra-cellular fluid is the medium surrounding the cells. It contains proteins, electrolytes, plasma and the interstitial fluid. The cell contains the protoplasm that contains the cytosol, the organelles and the nucleus of the cell as shown in figure 1.1 [1].

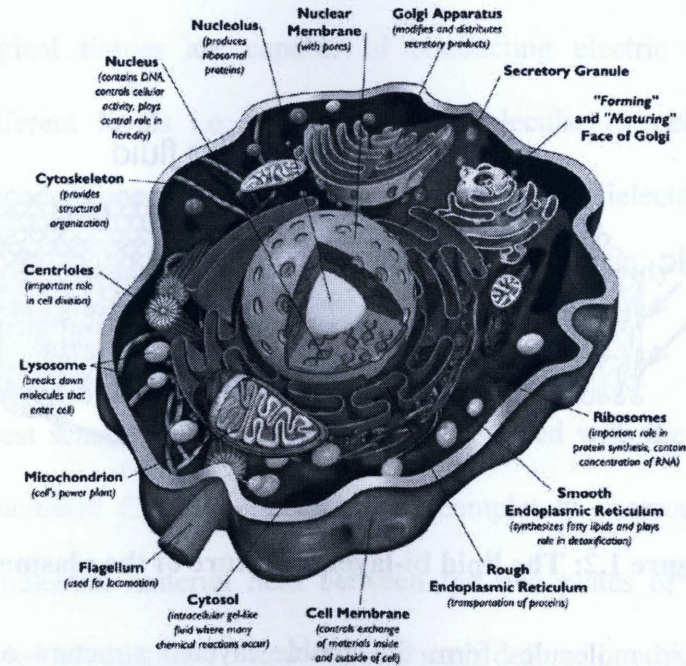


Figure 1.1: Biological cell and its constituents

1.1.1 Charge carriers in a tissue

Both the intra-cellular and extra-cellular fluids in a tissue contain electrolytes. The charge in an electrolyte is carried by the ions, unlike electrons in the metals. The positive charge carriers are called cations and the negative charge carriers are called anions. The total ionic conductivity of a solution depends on a number of factors e.g. concentration, activity, charge and mobility of all free ions in the solution. The most common ions contributing towards the ionic current are K^+ , Na^+ and Ca^{2+} . The ionic conductivity is also influenced by the viscosity and the temperature of the solution.

1.1.2 Cellular plasma membrane

The cell is completely enclosed in a plasma membrane that consists mainly of proteins and lipids. The plasma membrane is a thin and elastic structure with a width of roughly 100 Å.

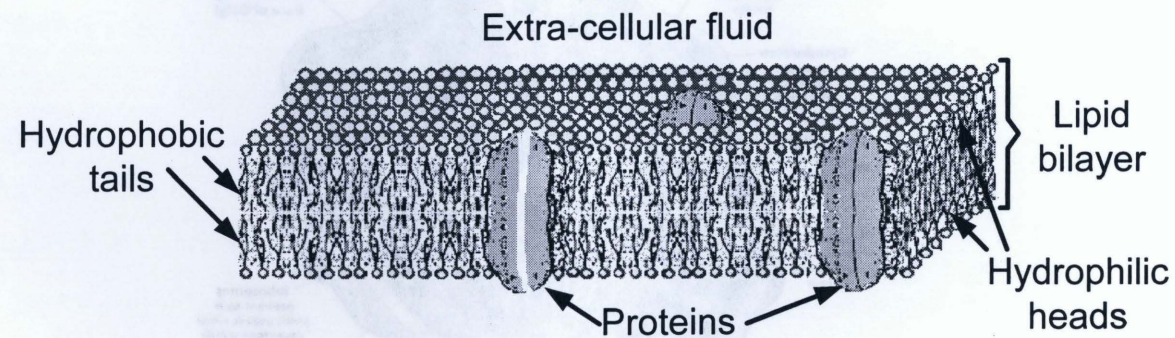


Figure 1.2: The lipid bi-layer structure of the plasma membrane

Two lipid molecules form the double layered structure of the plasma membrane which is repeated in every direction as shown in figure 1.2 [2]. Each lipid molecule has a

hydrophilic and a hydrophobic side. The hydrophobic sides attract each other and forces the hydrophilic head into the exterior and the hydrophobic into the interior of the structure.

The plasma membrane is considered as an insulator. The overall structure in a biological tissue formed by the intracellular fluid (conductor), plasma membrane (insulator) and extra-cellular fluid (conductor) acts as a capacitor.

The bi-layer structure contains proteins of various types. The proteins pass through the lipid bi-layer creating very narrow channels for ions and water to pass. When viewed electrically this acts as a resistive path which allows current to pass.

1.1.3 Tissue dielectricity and conductivity

Dielectricity of any material is defined as the ability to store capacitive energy and conductivity is defined as the ability to conduct an electric current in response to an applied field. The biological tissues are capable of conducting electric current and exhibit dielectricity at different levels i.e. molecular, sub-molecular or cellular. The plasma membrane of the cell is the major contributor towards the dielectric behaviour of the biological tissues. The conductivity mainly arises from the mobility of extra-cellular and intra-cellular ions.

In its simplest sense the dielectric theory is explained with the help of a capacitor. The electrical capacitance C and conductance G completely characterizes the electrical properties of the dielectric material held between the two plates of the capacitor. The conductance is defined in equation 1.1 and capacitance is defined in equation 1.2.

$$G = \frac{\sigma A}{d}, \quad (1.1)$$

$$C = \frac{\epsilon_o \epsilon_r A}{d}, \quad (1.2)$$

Where, σ denotes the electrical conductivity of the material, A denotes the surface area of the plates of capacitor, d denotes the distance between the plates, ϵ_o denotes the dielectric permittivity of free space and its value is 8.854×10^{-12} F/m, and ϵ_r denotes the permittivity of the material relative to ϵ_o .

The schematics of a typical capacitor with a plate surface area A ; separated by a dielectric of thickness d , is shown in figure 1.3(a). The equivalent circuit diagram is shown in figure 1.3(b).

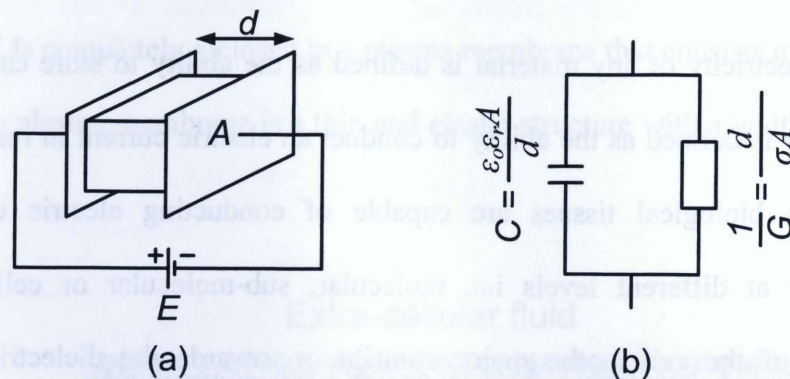


Figure 1.3 (a): Schematics of a typical capacitor, (b): Equivalent circuit diagram

If the applied voltage is sinusoidal then the electrical characteristics of the circuit in figure 1.3(b) varies with frequency and can be specified in several ways. At the excitation frequency ω , the complex admittance Y^* can be expressed as:

$$Y^* = G + j\omega C = \frac{A}{d}(\sigma + j\omega\epsilon_o\epsilon_r), \quad (1.3)$$

From which the complex conductivity σ^* , also called admittivity or specific admittance can be defined as:

$$\sigma^* = \sigma + j\omega\epsilon_o\epsilon_r, \quad (1.4)$$

Impedance which is defined as the inverse of the complex admittance can be written as:

$$Z^* = \frac{1}{Y^*} = R + jX = \frac{G - j\omega C}{G^2 + (\omega C)^2}, \quad (1.5)$$

From which the complex specific impedance z^* , also called impedivity of the material is defined as:

$$z^* = \frac{1}{\sigma^*} = \frac{\sigma - j\omega\epsilon_o\epsilon_r}{\sigma^2 + (\omega\epsilon_o\epsilon_r)^2} = \rho^*, \quad (1.6)$$

The complex specific impedance z^* is also called complex resistivity, and is denoted by ρ^* . For a skeletal muscle at 1 MHz, the conductivity is approximately ten times greater in magnitude than dielectricity [3]. So the dielectricity or the imaginary part of complex specific impedance can be neglected at 1 MHz.

1.1.4 Frequency dependence of impedance

A biological tissue is considered as a dispersive medium and both permittivity and conductivity are functions of frequency as shown in figure 1.4 [2]. This observed frequency dependence is called dispersion and it arises from several mechanisms as shown in [4]. Dispersions can be understood in terms of the orientation of the dipoles and the motion of ions. At relatively low frequencies, it is easier for the dipoles to orient in response to the changes in the applied field, whereas the ions travel larger distances over which a greater

opportunity exists for trapping at a defect or interface. Therefore at low frequencies, permittivity is relatively high and conductivity is relatively low. As the frequency increases, the dipoles are less able to follow the changes in the applied field and the corresponding polarization disappears. In contrast, the ions travel shorter distances during each half cycle and are less likely to be trapped. As the frequency increases the permittivity decreases and since trapping becomes less important the conductivity increases. Four dispersion regions are identified namely α -, β -, δ - and γ -dispersion.

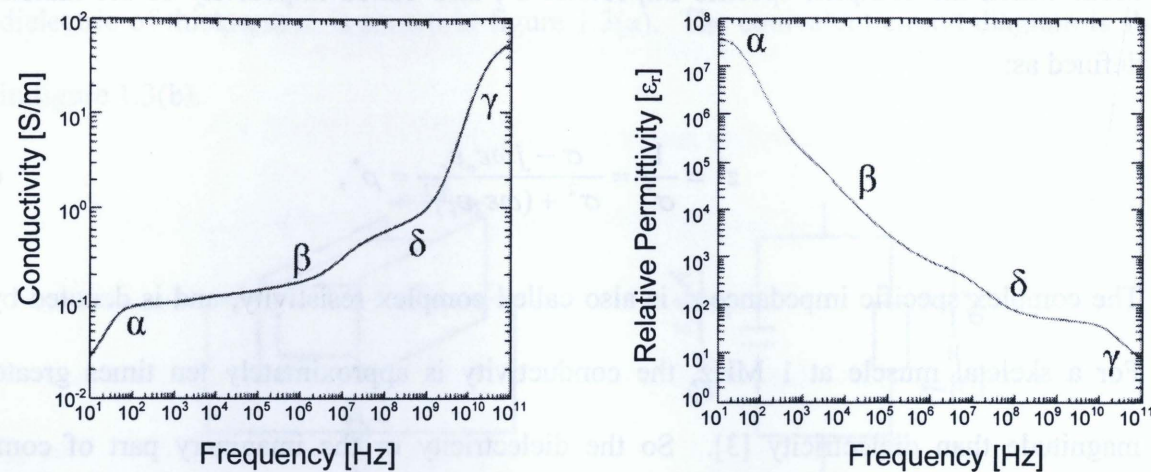


Figure 1.4: Frequency dependence of conductivity and permittivity in brain grey matter

The biochemical phenomena responsible for α -dispersion are still unknown. However, Foster and Schwan [4] suggested that α -dispersion, partly arises because of the counter-ion effect which is the formation of an electric double layer as a result of the ionic diffusion through the membrane. The ion passes through the narrow channels of the proteins as shown in figure 1.2. The characteristic frequency range of this dispersion is from 1 Hz to 10 kHz. The α -dispersion is because of the complete charging and discharging of the outer membrane of the cells. The current is not able to penetrate the lipid membrane but is only

able to diffuse through the narrow protein channels. Hence the total impedance of the tissue is large.

The β -dispersion occurs in the frequency range from 10 kHz to 100 MHz. The β -dispersion is because of the partial charging of the cell membrane. The current at these higher frequencies is able to flow through the lipid membrane, charging the small intracellular space structures. Hence in β -dispersion the total impedance of the tissue is smaller.

The δ -dispersion, centered at frequencies between 100 MHz and 1 GHz, is due to the relaxation of bound water molecules, small proteins, amino acids and protein side chains [4].

The γ -dispersion is centered at 20 GHz and is due to the dipole moment of free water molecules.

1.1.5 Equivalent circuit model of a biological cell

Considering the main constituents of the cell as introduced earlier and applying the theory of electric circuits, it is possible to deduce an equivalent electrical model of a cell as shown in figure 1.5(a) [2]. Figure 1.5(b) represents simplified cell model. The resistance R_m parallel to the capacitance C_m can be neglected, since its value is quite high. The model can further be simplified as shown in figure 1.5(c), where $C_i^* = \frac{C_m}{2}$.

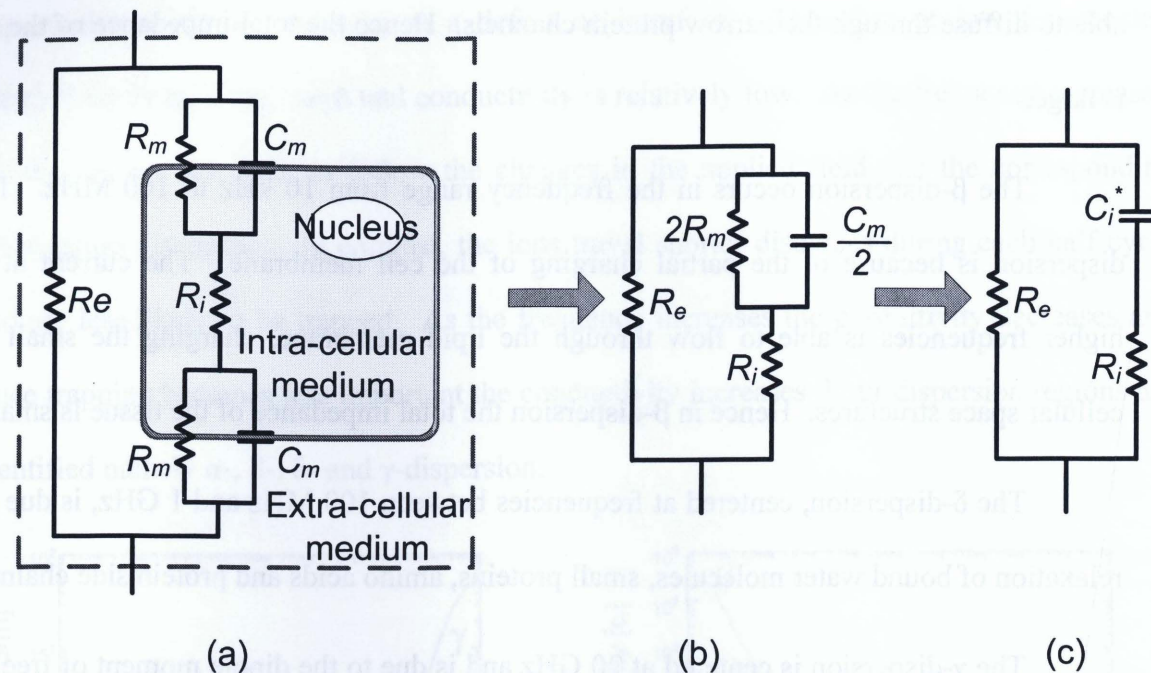


Figure 1.5 (a): Equivalent electrical circuit of a cell, (b): Simplified model, (c):

Simplified model after neglecting R_m

If the current is injected into the extra-cellular medium, it can:

- Flow around the cell through the extra-cellular fluid encountering the resistance R_e .
- Flow through the cell across the plasma membrane encountering the capacitance C_m .
- Or, flow across the trans-membrane ionic channel encountering a resistance of R_m .

Once the current is in the cell, it flows through the intra-cellular medium encountering the resistance R_i and leaving the cell through the plasma membrane which can be modeled as a parallel combination of R_m and C_m . Usually, the membrane conductance is very low, so the

effect of R_m is neglected and the equivalent circuit is very simple figure 1.5(c). The use of this simplified model is widespread and is used to explain impedance measurements in a broad range of frequencies from dc to a few tens of MHz.

At low frequencies near dc (i.e. α -dispersion), the plasma membrane acts as an insulator and the current is not able to penetrate the cell, and most of the current flows around the cell (represented as oval shaped object surrounded by extra-cellular fluid) as shown in figure 1.6.

The net tissue impedance is high in α -dispersion. The insulating effect of the cell membrane decreases with increasing frequency, and the current is able to flow through the cell (i.e. β -dispersion). At frequencies above 1MHz the membrane capacitance is not an impediment to the current and it flows indiscriminately through the intra- and extra-cellular regions and the overall impedance of the tissue decreases.

— Current path of low frequencies
 - - - Current path of high frequencies

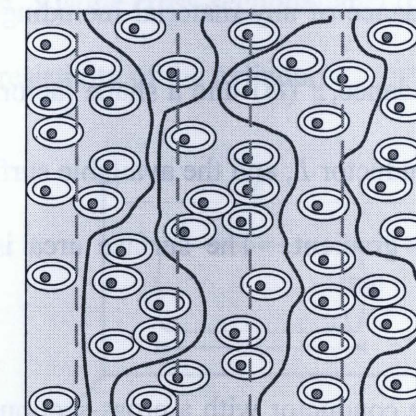


Figure 1.6: Paths of high and low frequency currents in a biological tissue

1.2 Electrical properties of a cancerous tissue

A tumor is an abnormal mass of tissue surrounded by normal body tissues. It has no useful function and grows at the expense of healthy tissues. There is evidence that the tumor tissues have higher water content than the corresponding normal tissues. A study by Smith [5] on liver tumours in the β -dispersion regime showed a significant difference in the electrical properties between healthy liver tissues and tumours. Results show that tumour conductivity is 6-7.5 times higher than normal liver conductivity; the difference in permittivity values is 2-5 times. However, the dielectric properties of tumours cannot be generalized as large differences exist between different tumour types and even between tumours of the same type. Electrical properties depend greatly on the size or the developmental stage of the tumour.

1.3 Electrical impedance of a tissue

The electrical impedance of any material including biological tissue is given by the product of its specific impedance, $z^*(\omega)$ and a shape factor, k . The shape factor depends on the length of the volume conductor L , and the available surface area S , for the electric current to flow due to a potential gradient. The surface area is normal to the direction of the gradient.

An arbitrary volume conductor with a cross-sectional area that varies along x-axis is shown in figure 1.7. The electrical impedance is given by:

$$Z(\omega) = z^*(\omega)k = z^*(\omega) \int_0^L \frac{dx}{S(x)}, \quad (1.7)$$

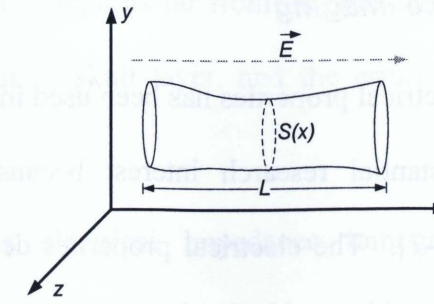


Figure 1.7: Volume conductor with specific impedance $z^*(\omega)$, length L , and cross-sectional area $S(x)$

In case of a pure resistive cylindrical conductor as shown in figure 1.8, with homogeneous (spatially invariant) resistivity independent of frequency, the total resistance R of the conductor along x-axis is given by:

$$R = \rho \frac{L}{S}, \quad (1.8)$$

Where L is the length, S is the cross-sectional area (normal to the electric field which is along x-axis) and ρ is the resistivity of the cylinder.

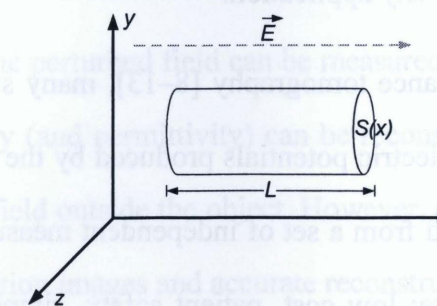


Figure 1.8: Cylindrical conductor with resistivity ρ , length L , and cross-sectional area S , normal to the electric field \vec{E}

1.4 Electrical impedance imaging

The imaging of electrical properties has been used in various clinical applications and continues to attract substantial research interest because of the functional nature of information it provides [6-7]. The electrical properties determine the pathways of current flow through the body and thus are very important in the analysis of a wide range of biomedical applications such as functional electrical simulation and the diagnosis and treatment of various physiological conditions with weak electric currents, radio frequency hyperthermia, electro-cardiography, and body composition. On a more fundamental level, knowledge of these electrical properties can lead to an understanding of the underlying basic biological processes.

There are several methods for imaging electrical impedance such as electrical impedance tomography (EIT), magnetic resonance electrical impedance tomography (MREIT), and magnetic induction tomography (MIT). Each of the above techniques has its strength and weakness. However, none of them can produce high-spatial-resolution images of electrical impedance for any application.

In electrical impedance tomography [8-13], many surface electrodes are attached to an object to measure the electric potentials produced by the injected currents. An impedance image can be reconstructed from a set of independent measurements of transfer impedances. The advantages of EIT are: low cost, patient safety, simplicity, rapid data collection, and potential for tissue characterization. The major disadvantage of EIT is that the spatial resolution is poor due to the ill-posedness of the corresponding inverse problem involved in image reconstruction. Other disadvantages include the low sensitivity of the surface voltage

to the conductivity changes in regions far from the electrodes, the shielding effect [14-17] due to low conductivity fat or skull layer, and the errors related with the placement of electrodes on the body [15].

Magnetic resonance electrical impedance tomography [18] is based on the measurements of current density distribution inside a subject body using magnetic resonance imaging (MRI). While the current is injected through the electrodes attached to the body surface of the subject, at the same time MR images are obtained using a spin-echo sequence synchronized with the current pulses. The magnitude of the current density mapping can be computed from MR images. After that, the current density data is utilized to reconstruct the static cross-sectional resistivity images. The internal current density data eliminate the sensitivity problem in conventional EIT image reconstruction. The disadvantages of MREIT include the shielding effect, high cost due to the use of MRI, and the safety issue due to the injection of relatively long current pulses (~ 40 ms) into the body.

Magnetic induction tomography [19-20] uses the interaction of an oscillating magnetic field with conductive media. The field excited by coils is perturbed by eddy currents in the object and the perturbed field can be measured by small coils arranged around the object. The conductivity (and permittivity) can be reconstructed from the measurements of the perturbed magnetic field outside the object. However, so far, MIT has not been able to produce high-spatial-resolution images and accurate reconstruction algorithms still need to be developed.

Hence, currently, there is no readily available imaging modality to produce high-resolution images of electrical conductivity of tissues for medical applications.

1.5 Hypothesis

The motivation behind MAET is to provide high-spatial-resolution current density information which can be useful in obtaining impedance distribution and hence differentiating normal and cancerous tissues.

MAET requires the mapping of the current density distribution J_{ab} that would exist in a sample if a current/voltage source were to be applied directly through measurement electrodes a and b as shown in figure 1.9. Electrical impedance can thus be calculated from current density distribution J_{ab} . In order to map $J_{ab}(r)$ (current density at any point r) experimentally, i.e. without directly applying a current/voltage source, the sample is placed in a static magnetic field and an ultrasonic pulse is focused on the sample to simulate a point like current dipole source at r as shown in figure 1.10. The vibrations of ions in the sample caused by the ultrasound can induce an electric current distribution via the Lorentz force mechanism. Consequently, a voltage/current can be measured through electrodes [21-24]. It will be shown in chapter 2 that the measured voltage/current is proportional to a component of $J_{ab}(r)$ based on the reciprocity theorem of electromagnetic waves [25]. Mapping of J_{ab} is accomplished by scanning an ultrasound beam throughout the sample. The electrical impedance of the sample may be reconstructed from J_{ab} .

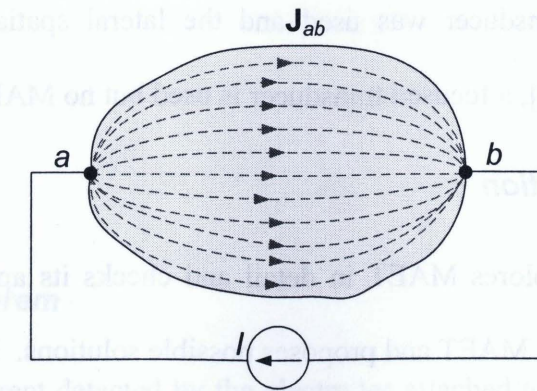


Figure 1.9: Illustration of lead field current density distribution in a sample

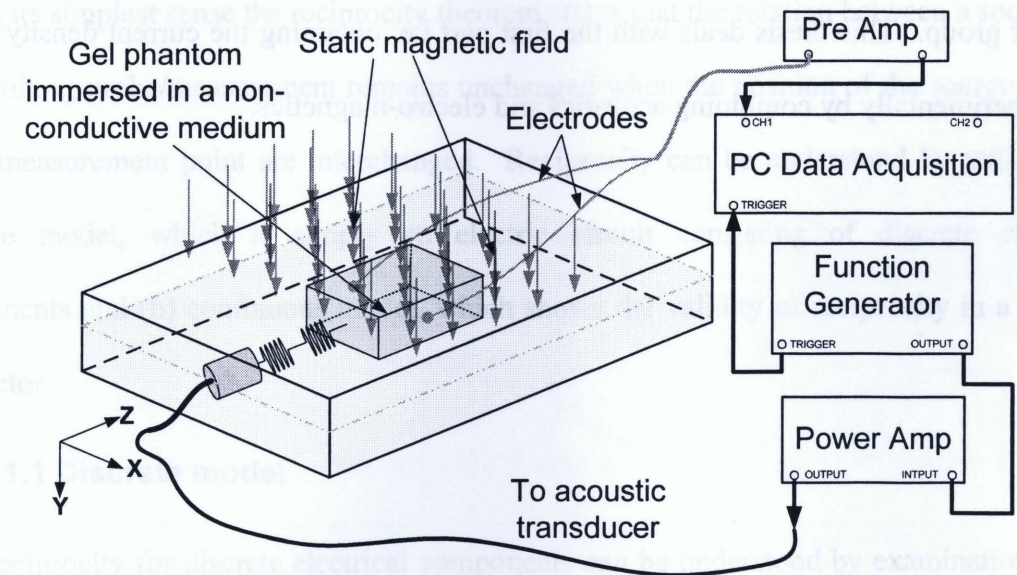


Figure 1.10: Schematics of MAET experimental setup

1.6 Previous studies similar to MAET

The idea of combining ultrasound and magnetic field to image electrical properties of tissues has been reported in the literature [22-23]. Although an image is given in Wen's

paper [22], a flat transducer was used and the lateral spatial resolution was poor. In Montalibet's paper [23], a focused transducer is used but no MAET image is shown.

1.7 Thesis contribution

This thesis explores MAET in detail and checks its applicability to image tissues, discusses challenges in MAET and proposes possible solutions. In order to obtain impedance information by using this technique, the first part is to obtain the current density distribution, the second part is to solve for conductivity from the measured current density distribution. The second part is called the inverse problem and is studied by another graduate student in our group. This thesis deals with the first part i.e. obtaining the current density distribution experimentally by combining acoustics and electro-magnetics.

Chapter 2

Theory

2.1 Reciprocity theorem

The voltage/current detected by the electrodes attached to the sample is proportional to a component of J_{ab} . This can be shown using the *Reciprocity Theorem* of electromagnetics [26-27].

In its simplest sense the reciprocity theorem states that the relation between a source and the resulting probe/measurement remains unchanged when the position of the source and the probe/measurement point are interchanged. Reciprocity can be understood by utilizing (a) discrete model, which is simply an electric circuit consisting of discrete electrical components and (b) continuous model, which shows the validity of reciprocity in a volume conductor.

2.1.1 Discrete model

Reciprocity for discrete electrical components can be understood by examination of the two circuits shown in figure 2.1. In circuit 1, the 5 V source in branch A produces a current I_1 equal to 0.147 A in branch B. In circuit 2, the 5 V source is moved to branch B which produces a current I_2 equal to 0.147 A in branch A. The equality of both the currents I_1 and I_2 is due to the reciprocity.

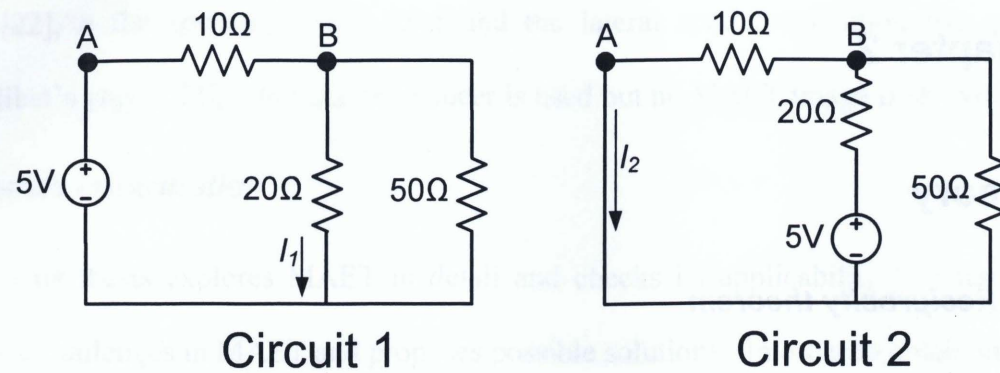


Figure 2.1: Reciprocity for discrete electrical circuit

2.1.2 Continuous model

Reciprocity for a continuous model can be understood by looking at two volume conductors as shown in figure 2.2.

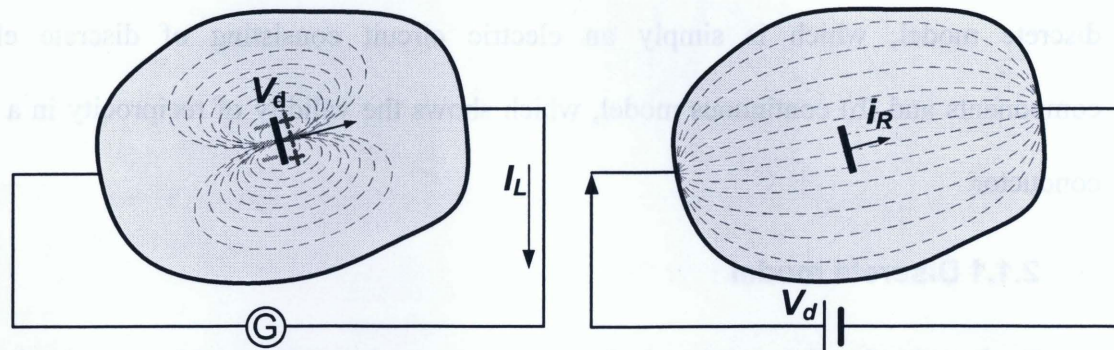


Figure 2.2: Reciprocity for volume conductor

In the left diagram of figure 2.2, a galvanometer G is connected at the surface of the volume conductor. Inside the conductor is a thin double layered source representing a dipole across which the voltage is V_d and which causes a current I_L in the galvanometer circuit. In the right diagram of figure 2.2, the double layered source is removed from the volume conductor and the galvanometer is replaced by an electromotive source of the same

magnitude V_d . This produces a reciprocal current i_R through the same cross-section where the double layered source had been located. According to the reciprocity theorem $I_L = i_R$ [28].

Reciprocity for a volume conductor is the basis for MAET. In order to measure the current density at a given point in a biological tissue, it is not necessary to measure it directly by invasively placing a current probe at the location. Instead, a “point battery” can be generated at the same location, no-invasively, by a combination of static magnetic field and a focused ultrasound. The voltage/current produced by this “point battery” can be measured at the boundary of the tissue.

2.2 Derivation of the fundamental equation

Assuming that two independent impressed electric fields E'_1 and E'_2 (where prime indicates the impressed/source term) induces two independent current distributions J_1 and J_2 respectively in the same conducting sample.

The first field E'_1 and the associated current distribution J_1 , represents a MAET configuration, in which an ultrasound is focused at a point r in the sample which is located in the static magnetic field. The Lorentz force mechanism $E'_1 = v \times B_o$ can be considered as an applied (impressed) electric field which induces an electric field of E_1 in the sample, where v is the vibration velocity of ions in the ultrasound field and B_o is the static magnetic field. The total current density is given by [25], [29]:

$$J_1 = \sigma^*(E_1 + v \times B_o), \quad (2.1)$$

Where $\sigma^* = \sigma + j\omega\epsilon_o\epsilon_r$, σ^* is the complex conductivity or admittivity, σ is conductivity, ω is the frequency of electrical field, and ϵ_o and ϵ_r are permittivity of free space and relative permittivity respectively.

Assume that the measured current through the electrodes at r_a and r_b is I as shown in figure 1.9, hence:

$$\nabla \cdot J_1 = I[\delta(r - r_a) - \delta(r - r_b)], \quad (2.2)$$

For the second impressed electric field E'_2 and the associated current distribution J_2 , there is neither ultrasound nor B_o . Instead, a hypothetical voltage $V_o = \phi'_a - \phi'_b$ is applied through the two measurement electrodes as shown in figure 1.9. Where ϕ'_a and ϕ'_b are the electrical potentials at the two electrodes.

According to reciprocity theorem the volume integral is given by [25],

$$\int_V (J_1 \cdot E'_2 - J_2 \cdot E'_1) dv = 0, \quad (2.3)$$

Where, V is the volume of conductor. Substitution of **Error! Objects cannot be created from editing field codes.** in the above integral gives:

$$\int_V (J_1 \cdot E'_2 - (v \times B_o) \cdot J_2) dv = 0, \quad (2.4)$$

Assuming that the current J_1 vanishes at the boundary and that $E'_2 = -\nabla\phi'_2$, the above integral becomes:

$$\int_V (J_1 \cdot E'_2) dv = \int_V (\phi'_2 (\nabla \cdot J_1)) dv, \quad (2.5)$$

After substituting equation 2.2 in 2.5 and integrating over the volume, the final expression is:

$$I = \frac{\int_V [(v \times B_o) \cdot J_2] dv}{V_o}, \quad (2.6)$$

In the experiments the voltage detected across the electrodes can also be measured. To derive the relationship between the measured voltage V_m and the acoustic field, the sample is treated as a voltage source with an internal resistance of R and a voltage drop of IR , where R is the impedance of the sample measured from the two electrodes. Assuming that the input impedance of voltmeter is much higher than R , the measured voltage is approximately equal to IR . Equation 2.6 can now be written as:

$$V_m = \frac{\int_V [(v \times B_o) \cdot J_2] dv}{I_o}, \quad (2.7)$$

Where I_o is the current through the sample when V_o is applied to the electrodes. The above equation can further be simplified to:

$$V_m = \int_V [(v \times B_o) \cdot J_{ab}] dv \quad (2.8)$$

Where J_{ab} is the resulting current density distribution in the sample, if a current of 1 Ampere is injected in to the sample through the measurement electrodes a and b as shown in figure 1.9. This expression is also given in Wen's paper [21]. The voltage expression given by equation 2.8 will be used throughout the thesis, since a voltage preamplifier is used in the experiments.

Both v and B_o in equation 2.8 are approximately independent of the type of tissue sample and can be determined in advance. If an ultrasound is focused on the tissue, the vibration velocity v can be localized to a small volume in space as shown in figure 2.3. The length and cross-section of this volume are determined by the ultrasound pulse width and the beam diameter respectively. This small volume is moving along the ultrasound transducer axis at the speed of sound. Consequently, the measured voltage corresponds to the integration of $(J_{ab})_{v \times B_o} = n_{v \times B_o} \cdot J_{ab}$ over the small volume, where $n_{v \times B_o}$ is the unit vector pointing in the direction of $v \times B_o$; i.e. the measured voltage (MAET signal) is proportional to the component of J_{ab} in the direction of $v \times B_o$. Therefore $(J_{ab})_{v \times B_o}$ can be measured at a spatial resolution which is approximately equal to the dimension of the ultrasound beam.

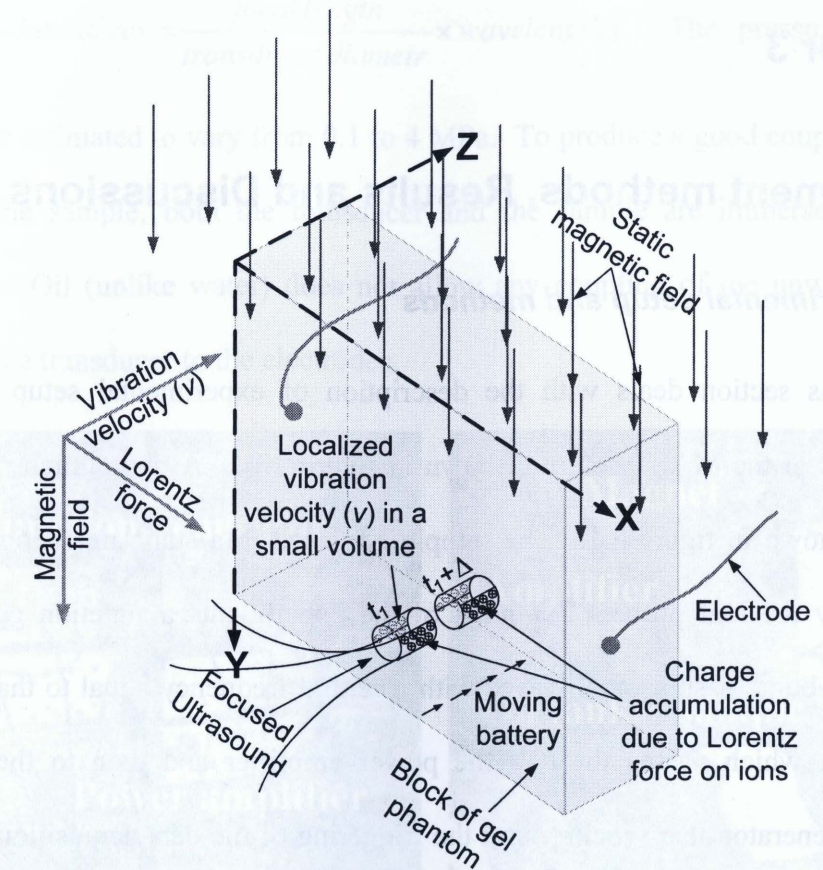


Figure 2.3: Generation of MAET signal in a thick block of gel phantom

The above analysis assumes that the voltage/current is measured by the electrodes attached to the sample. However, the analysis can be generalized to include other measurement methods. For example, a coil can be used to measure the time varying magnetic field associated with the $v \times B_o$ current generated in the sample. In this case, J_{ab} is the current density distribution induced in the sample if a current of 1 Ampere is applied through the two coil terminals, a and b . This method is more convenient and robust in practice because no electrodes need be attached to the sample. In addition, this configuration can provide more options for impedance reconstruction algorithms.

Chapter 3

Experiment methods, Results and Discussions

3.1 Experimental setup and methods

This section deals with the description of experimental setup for MAET. The schematics of the MAET setup is shown in figure 1.10. A photograph of the experimental setup is shown in figure 3.1. The sample is placed in a static magnetic field of 0.2-0.3 T verified by the hall probe. For most of the experiments a function generator is used to generate a burst of sinusoidal waves with a central frequency equal to that of the ultrasound transducer, which passes through the power amplifier and then to the transducer. The function generator also synchronizes the triggering of the data acquisition card attached to a PC and the excitation of the transducer. The voltage detected by the electrodes is amplified before the data acquisition. As shown in figure 1.10, the ultrasound beam transmitted by the transducer strikes perpendicularly on the face of the sample, this is essential in MAET in order to produce a stronger signal. Since the total MAET signal is the summation of all individual signals produced by each point of the sample in the ultrasound beam. The spatial extent of the pulse along the transducer axis (or the wave propagation direction) defines the axial resolution (i.e. the resolution along the transducer beam). If the transducer produces a burst of duration τ_p , then the axial resolution is given by $l_p = v_s \tau_p$, where $v_s = 1.5 \text{ mm}/\mu\text{s}$ is the speed of the ultrasound in water or soft tissues. The lateral resolution (i.e. the resolution perpendicular to the transducer beam) is determined by the ultrasound beam width

($\text{Beam width} = \text{lateral res.} = \frac{\text{focal length}}{\text{transducer diameter}} \times \text{wavelength}$). The pressure used in the

experiments is estimated to vary from 0.1 to 4 MPa. To produce a good coupling of acoustic waves with the sample, both the transducer and the sample are immersed in a tank of vegetable oil. Oil (unlike water) does not allow any coupling of the unwanted electrical signals from the transducer to the electrodes.

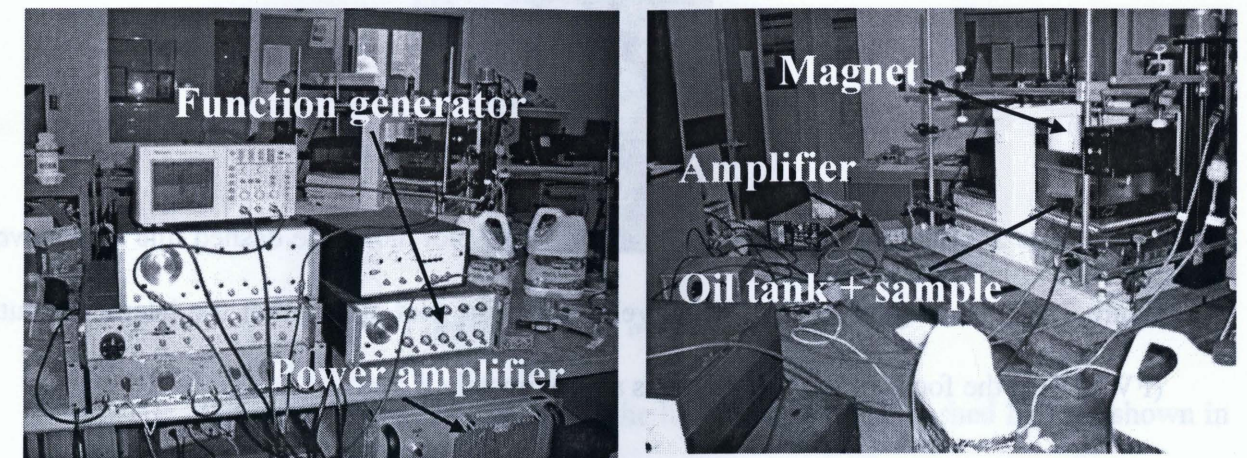


Figure 3.1: Actual MAET experimental setup

3.2 Field profile of the transducers

MAET experiments were performed by using two types of transducers; one with a central frequency of 1 MHz and the other with 2.25 MHz. The characteristics and the field profiles at the focus of both transducers are given in the following sub-sections. The field profiles of both transducers are obtained by scanning a hydrophone in the focal plane with a step size of 0.5 mm both in the x and y directions.

3.2.1 Field profile of 1 MHz transducer

Type:

Wide band

Focal length: 10.16 cm

Aperture diameter: 2.54 cm

$F^\#$ (= focal length/aperture diameter): 4



Figure 3.2: 1 MHz transducer

The 2D field profile at the focus and the line plot along the dashed line are shown in figure 3.3(a) and figure 3.3(b) respectively. The line plot shows that the lateral resolution (FWHM) at the focus of the transducer is approximately 8 mm.

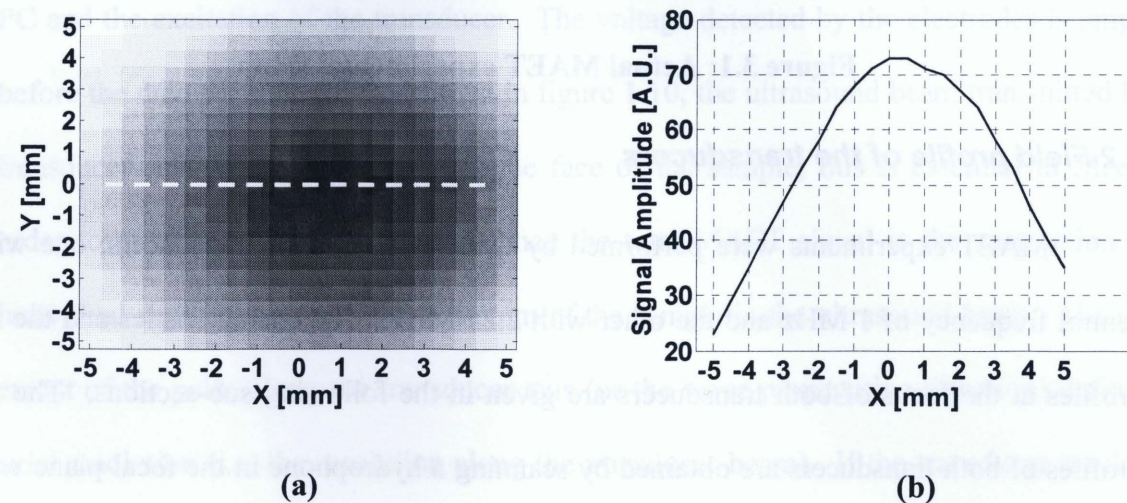


Figure 3.3 (a): Field profile of 1 MHz transducer at the focus (b): Line plot along the dashed line

3.2.2 Field profile of 2.25 MHz transducer

Type: Narrow band

Focal length: 10.16 cm

Aperture diameter: 5.08 cm

$F^\#$ (= focal length/aperture diameter): 2

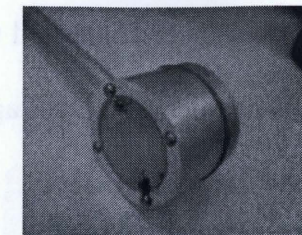


Figure 3.4: 2.25 MHz transducer

The 2D field profile at the focus and the line plot along the dashed line are shown in figure 3.5(a) and figure 3.5(b) respectively. The lateral resolution is approximately 4 mm.

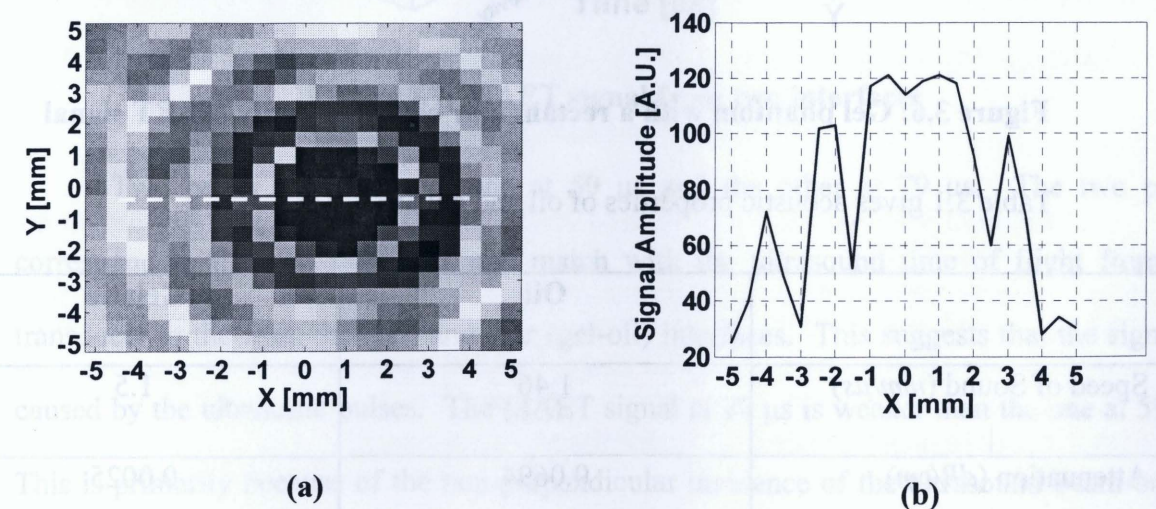


Figure 3.5 (a): Field profile of 2.25 MHz transducer at the focus (b): Line plot along the dashed line

3.3 Verification of MAET signals

The MAET signal (i.e. measured voltage) is first verified by using a thick gel phantom sample as shown in figure 3.6. By thick it means, that the dimension of the sample along the ultrasound propagation axis (i.e. z-axis) is much larger than the wavelength of the ultrasound in gel which is 1.5 mm for 1 MHz transducer. The sample has a 1 cm x 2 cm x 0.8 cm rectangular cavity in the middle. When the sample is placed in the oil, that cavity is filled up by the oil. A 1 MHz transducer connected to a function generator produces 2 μ s duration ultrasonic pulses. The time trace of the voltage detected by the electrodes is related to the current density profile along the sound path.

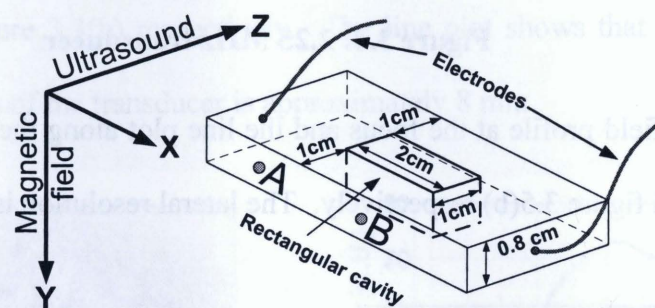


Figure 3.6: Gel phantom with a rectangular cavity to verify MAET signal

Table 3.1 gives acoustic properties of oil and gel at 1 MHz.

	Oil	Gelatin
Speed of Sound ($mm/\mu s$)	1.46	1.5
Attenuation (dB/cm)	0.0694	0.0025

Table 3.1: Acoustic properties of oil and gel at 1 MHz

3.3.1 MAET signal from a single point

When the ultrasound is incident at point A on the sample shown in figure 3.6, it travels throughout the thick sample without encountering the cavity. The MAET signal obtained is shown in figure 3.7. The MAET signal is recorded from the interface of two mediums with different conductivities. The reason behind it will be explained later.

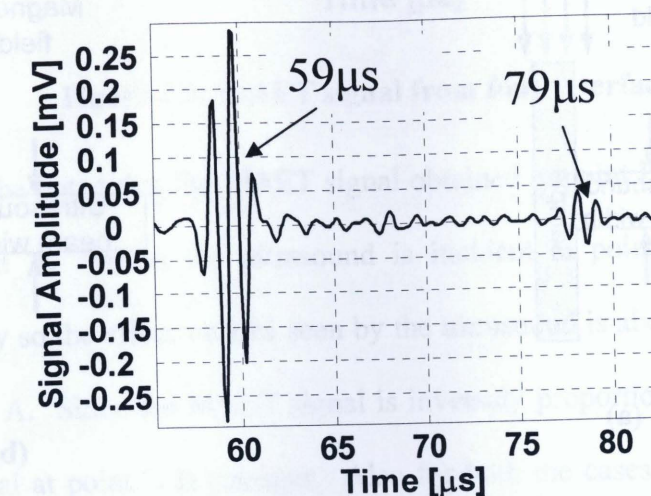


Figure 3.7: MAET signal from two interfaces

Two peaks are observed, one at 59 μ s and the other at 79 μ s. The two peaks correspond to the two interfaces and match with the ultrasound time of flight from the transducer to the front (oil-gel) and rear (gel-oil) interfaces. This suggests that the signal is caused by the ultrasonic pulses. The MAET signal at 79 μ s is weaker than the one at 59 μ s. This is primarily because of the non-perpendicular incidence of the ultrasound beam on the rear face of the sample. The ultrasound pulse also attenuates as it travels through the gel but the non-perpendicular incidence is the main reason behind the weakening of the pulse. As

discussed the MAET signal at a given transducer position is the summation of all individual signals produced by each point of the sample in the ultrasound beam. If the ultrasound strikes perpendicularly on the sample (figure 3.8(a)), then the signal from each point in the ultrasound beam adds up constructively giving a stronger signal and when the ultrasound strikes at an angle (figure 3.8(b)), the signals from each point of the sample in the ultrasound beam may cancel each other resulting in a weaker signal.

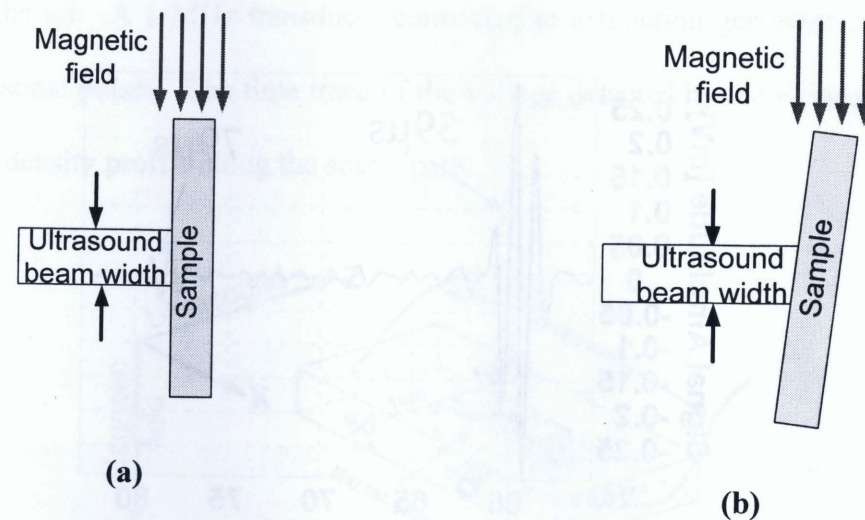


Figure 3.8 (a): Perpendicular ultrasound incidence gives stronger signal (b): Angular ultrasound incidence gives weaker signal

Figure 3.9 shows the MAET signal obtained when ultrasound is incident at point B. In this case the ultrasound encounters the rectangular cavity in the sample. Four peaks are observed that corresponds to the four interfaces. The strength of the signal decreases for each successive interface due to the same reasons as discussed above.

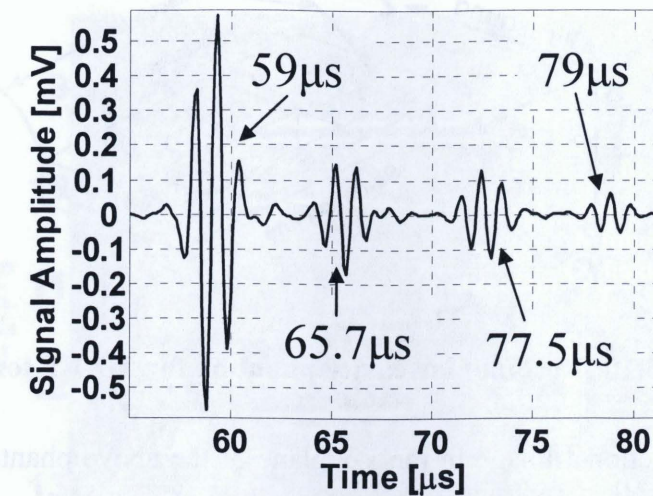


Figure 3.9: MAET signal from four interfaces

It should be noted that the MAET signal obtained at point B is stronger than the one obtained at point A. When the ultrasound is incident at point B it goes through the rectangular cavity so the effective area seen by the ultrasound is about $2/3^{\text{rd}}$ of the area when incident at point A. Since the MAET signal is inversely proportional to the cross-sectional area, so the signal at point B is stronger. Also for both the cases, the signals are obtained only from the interfaces and not from the homogeneous interior part of the sample.

3.3.2 MAET images

To obtain a tomographic MAET image, a gel phantom with the geometry shown in figure 3.10 is used. The 1 MHz transducer is scanned along the dotted line on the front face of the sample with a step size of 2 mm. The scanned cross-section lies roughly at the mid of the phantom thickness along y-axis.

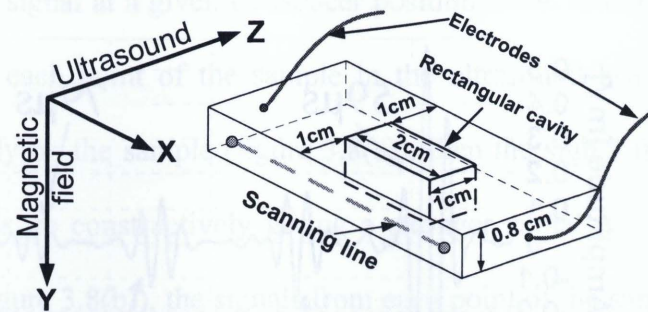


Figure 3.10: Rectangular cavity phantom for MAET tomography

The cross-sectional image in the x-z plane of the above phantom is shown in figure 3.11. This image is obtained by placing the time trace of the voltage signal (along z-axis) for each scanned point (along x-axis) side by side. The cross-sectional geometry in the tomographic image is in agreement with the original geometry. This image clearly shows that MAET signal is obtained only from the interfaces of the two mediums of different conductivities, and not from the homogeneous interior part. The rear boundary is not straight and bulges out beneath the cavity as shown between the dotted lines. This is because the ultrasound velocity in oil is smaller than in gel. So the net travel time for the ultrasound that travels in both gel and cavity is higher than the one that travels in gel only.

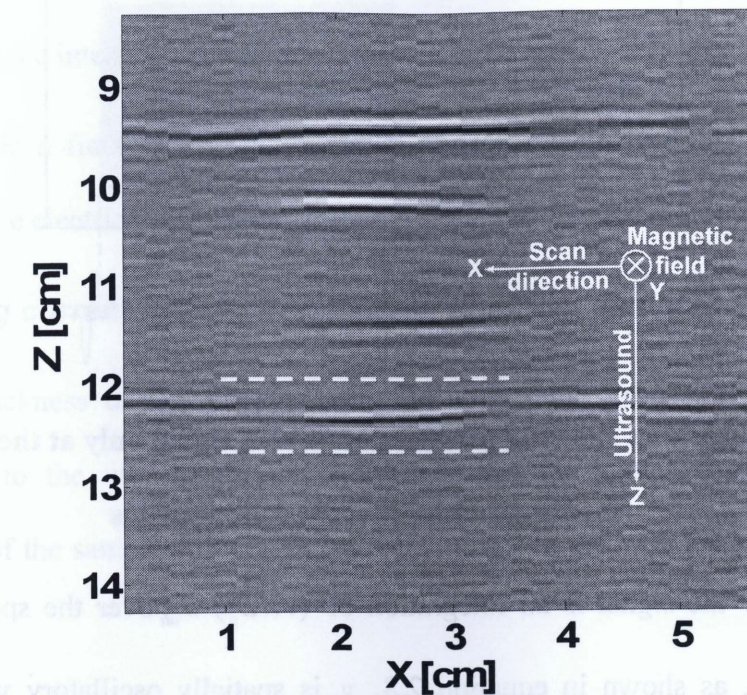


Figure 3.11: Tomographic MAET image of a rectangular cavity phantom

3.3.3 Cancellation of MAET signals in the interior of the sample

As discussed previously, the MAET signal is detected only at the interface of two mediums with different conductivities and no obvious signal is present in the homogeneous interior part of the sample, this is depicted schematically in figure 3.12. In the homogeneous part of the sample, the signal is too weak and is overwhelmed by the background noise.

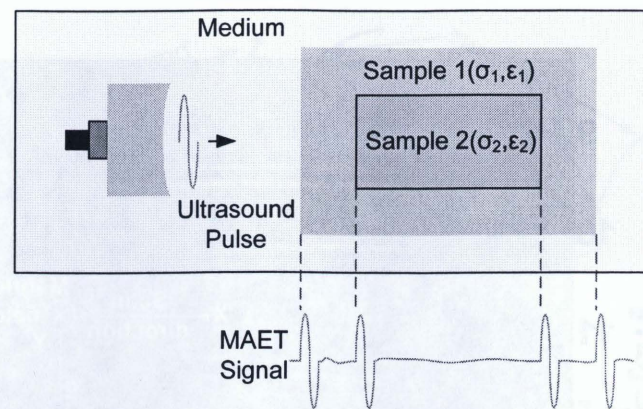


Figure 3.12: Schematics showing presence of MAET signal only at the interface of two mediums with different conductivities

In MAET the signal is an integration of $(\mathbf{v} \times \mathbf{B}_0) \cdot \mathbf{J}_{ab}$ over the spatial extent of the ultrasound pulse, as shown in equation 2.8. \mathbf{v} is spatially oscillatory with the period of ultrasound wave. The transducer in the experiments is driven by a sinusoidal wave, so the integration of \mathbf{v} over the spatial extent of the ultrasound pulse is zero because of the positive and negative half cycles of the sinusoidal wave. Within the spatial extent of the pulse \mathbf{B}_0 can be considered uniform. \mathbf{J}_{ab} also changes gradually in space, except at the interfaces between regions having different conductivities. Consequently, when the ultrasound pulse propagates within a uniform part of the sample, the integration of $(\mathbf{v} \times \mathbf{B}_0) \cdot \mathbf{J}_{ab}$ over the spatial extent of the ultrasound pulse reduces to a value proportional to the integration of \mathbf{v} over the spatial extent of the ultrasound pulse, and this latter integration results in zero. Therefore, this oscillatory nature of the ultrasonic wave renders a signal that is very small inside the homogeneous part of the sample. At the interface of regions having different conductivities, there is a step change in \mathbf{J}_{ab} , which yields an integration of $(\mathbf{v} \times \mathbf{B}_0) \cdot \mathbf{J}_{ab}$ over the spatial extent of the ultrasound pulse that is much larger than that of the non-boundary points (i.e.

interior of the sample). Therefore, MAET signals are only observed when the ultrasound pulse crosses the interfaces [22-24].

This is a fundamental limitation of MAET which needs to be solved in order to reconstruct the electrical impedance from current density at every point of the sample.

3.4 Imaging current density in a thin gel phantom sample with MAET

If thickness of the sample along the ultrasound propagation axis (i.e. z-axis) is comparable to the wavelength of ultrasound then the signals from the front and rear boundaries of the sample will merge into one pulse. In the case the sample is considered to be thin.

3.4.1 2D MAET image - experimental

The geometry of the thin sample is shown in figure 3.13. It has two wide regions and a narrow strip in the middle. The thickness of the sample along z-axis is approximately 2 mm.

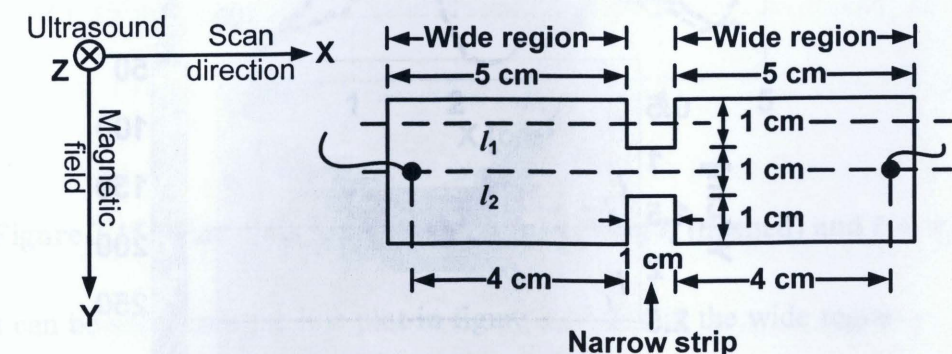


Figure 3.13: Sample geometry for thin gel phantom

For the above sample the current density is approximately uniform along the z-axis. Assuming that v and B_o in equation 2.8 do not change during the scanning. Then the amplitudes of the signals at the instant when the ultrasound pulse reaches the sample can be used to represent the current density at the focal point of the ultrasound. A 2.25 MHz transducer connected to a function generator is used to generate an ultrasound burst with a full width half maximum pulse length of about 5 μ s. Table 3.2 gives acoustic properties of oil and gel at 2.25 MHz.

	Oil	Gelatin
Speed of Sound ($mm/\mu s$)	1.46	1.5
Attenuation (dB/cm)	0.156	0.01

Table 3.2: Acoustic properties of oil and gel at 2.25MHz

Figure 3.14 shows the image of J_{ab} obtained by raster scanning the transducer in x-y plane.

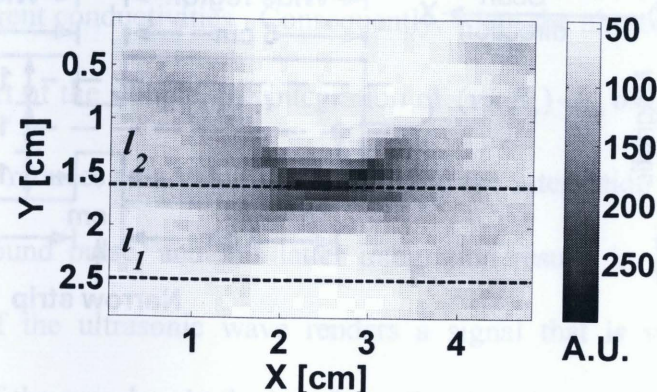


Figure 3.14: Image of J_{ab} from experiment. Lines l_1 and l_2 represents two scan levels

Figure 3.15 shows the plot of J_{ab} along the two dotted lines in figure 3.13 and figure 3.14. The solid line in figure 3.15 corresponds to line l_2 and shows that the current density at point A in the narrow strip ($X \sim 2.5$ cm) is about three times the value at point B ($X \sim 1$ cm) and point C ($X \sim 3.75$ cm), both of which are in the wider region. This agrees with the 1:3 ratio between the heights of the sample at the narrow and wider portions of the sample along y-axis. Since the area of the narrow strip is three times smaller than area of the wide region therefore the current density in the narrow strip is three times larger than the wider area. The dashed line corresponds to line l_1 and shows that the current density drops to noise level in the center region because the focal point is within the insulating oil where J_{ab} should be zero.

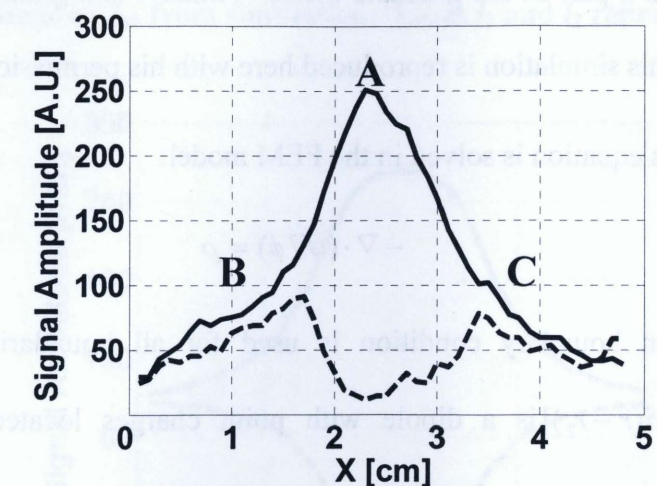


Figure 3.15: Line plots of J_{ab} in figure 3.14 along l_1 (dashed) and l_2 (solid)

It can be seen from the line plot in figure 3.15 that in the wide region of the sample (from 0-1.5 cm and 3.5-5 cm along X) the MAET signal does not remain at a constant level, but it either gradually increases or decreases as the transducer scans towards or away respectively from the narrow strip. This is because the magnetic field of the magnet is not

uniform. Magnetic field has a maximum magnitude of 0.3 T at the center which gradually reduces towards the edges which was confirmed by a magnetometer. The thin sample for this experiment is placed directly under the magnet in such a way that the center of the magnet coincides with the center of the sample. Therefore the MAET signal gradually decreases for the regions away from the center of the magnet/sample.

3.4.2 2D MAET image - numerical simulation

In order to verify the current density obtained experimentally, the finite element method (FEM) is used to simulate the current density distribution in a pure resistive sample having the same geometry as shown in figure 3.13. The numerical simulation is the work of Andrew Hrbek, and a part of his graduate thesis. Andrew is a graduate student working in the same group. This simulation is reproduced here with his permission.

The Poisson equation is solved in the FEM model:

$$-\nabla \cdot (\sigma \nabla \phi) = \rho \quad (3.1)$$

A Neumann boundary condition is used for all boundaries i.e. $J \cdot n = 0$, where $\rho = \rho_o [\delta(r - r_1) - \delta(r - r_2)]$ is a dipole with point charges located at positions r_1 and r_2 within the sample or on the boundaries, to account for the injected current. This approach serves to visualize the current density throughout the volume of the sample as the geometry is non-trivial and analytical solutions for the Poisson equation are available only for simple geometrical configurations.

Figure 3.16 and figure 3.17 show the corresponding results from the numerical simulation. J_{ab} is simulated with FEM by using COMSOL Multiphysics software. The numerical results agree fairly well with those from the experiments.

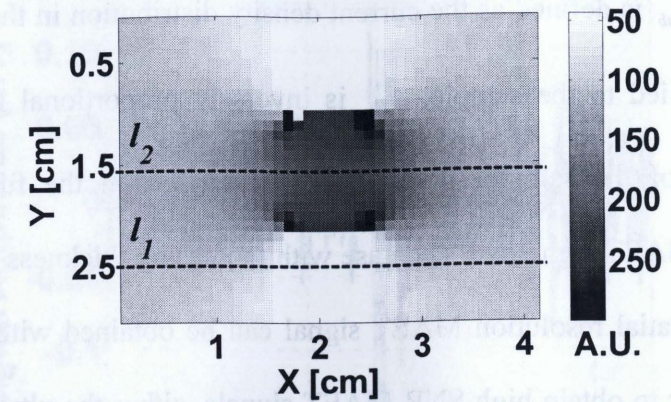


Figure 3.16: Image of J_{ab} from simulation. Lines l_1 and l_2 represents two scan levels

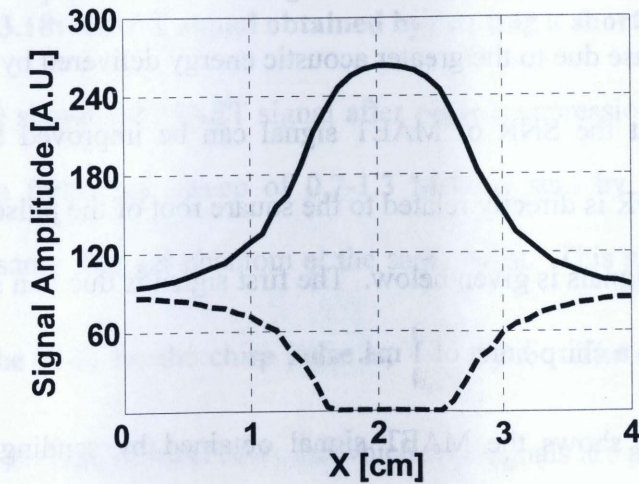


Figure 3.17: Line plots of J_{ab} in figure 3.16 along l_1 (dashed) and l_2 (solid)

A comparison of experimental (figure 3.14) and simulation (figure 3.16) images of J_{ab} reveal some discrepancies. This may be due to the non-uniformity of saline concentration in the sample or due to the non-perpendicular incidence of ultrasound on the sample face. Also

the simulation is performed with a uniform magnetic field so there is no weakening of MAET signal away from the center of the magnet as shown in figure 3.17.

3.4.3 Improvement of SNR by CHIRP

Since J_{ab} is defined as the current density distribution in the sample if a current of 1 Ampere is applied to the sample, J_{ab} is inversely proportional to the thickness or cross sectional area of the sample; this can be deduced from the fundamental equation 2.8. Therefore the MAET signal will decrease with increasing thickness of the sample. For a thin sample, high spatial resolution MAET signal can be obtained with high SNR. For a thick sample, in order to obtain high SNR MAET signals, either the ultrasound pressure has to be increased or a long ultrasound chirp burst would be used and the data would be processed by the pulse compression techniques to obtain high axial resolution [30-31]. In the second case, the SNR will increase due to the greater acoustic energy delivered by the longer pulse. It will be now shown that the SNR of MAET signal can be improved by using chirp and that improvement in SNR is directly related to the square root of the pulse length. Comparison of the SNR's of two signals is given below. The first signal is due to a short pulse of 2 μ s while the second is due to a chirp burst of 1 ms.

Figure 3.18 shows the MAET signal obtained by sending a short pulse of 2 μ s duration from a 1 MHz transducer to a thin gel phantom (~ 2 mm thick) at a single point. The signal is obtained after averaging 100 times in time domain. The SNR after 100 times averaging is, $\frac{0.25 \times 10^{-3}}{0.1 \times 10^{-3}} = 2.5$. The numerator is the peak-to-peak value of the signal at 60

μ s in figure 3.18 and denominator is the peak-to-peak value of the back ground noise.

Therefore the actual SNR without any averaging would be, $\frac{2.5}{\sqrt{100}} = 0.25$.

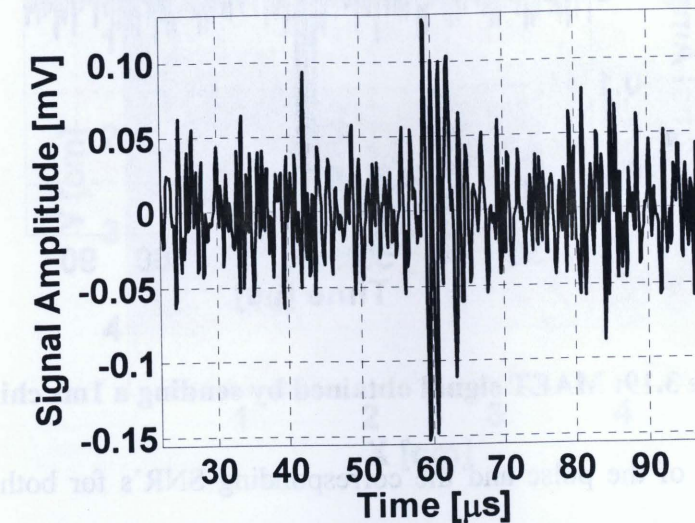


Figure 3.18: MAET signal obtained by sending a short pulse of 2 μ s

Figure 3.19 shows the MAET signal after pulse compression, when a 1 ms duration chirp pulse with a frequency sweep of 0.7-1.3 MHz is sent by using the same 1 MHz transducer on the same thin gel phantom at the same point. This signal is obtained without any averaging. The SNR for the chirp pulse is, $\frac{0.45}{0.08} = 5.6$. The signal processing for the pulse compression is done in MATLAB for which two signals are acquired. The first one is the 1 ms duration chirp pulse, which is acquired directly from the function generator and is called the reference signal. The second signal is the MAET signal acquired from electrodes attached to the sample. Both the reference and the electrode signals are cross-correlated with the MATLAB built-in function to produce a compressed signal as shown in figure 3.19.

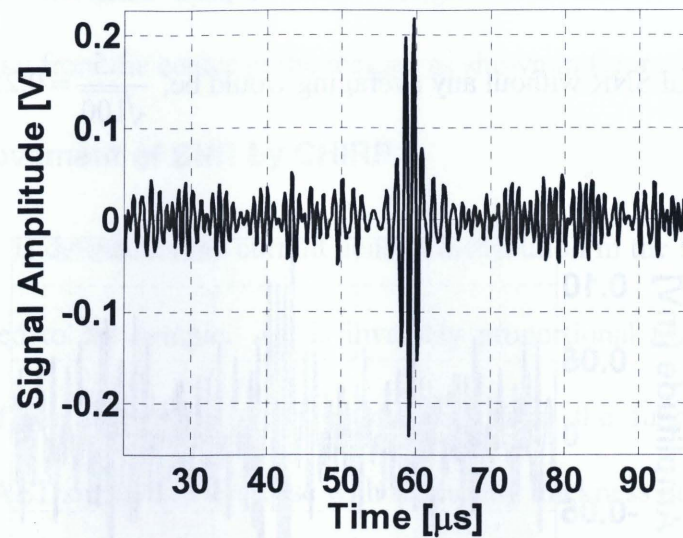


Figure 3.19: MAET signal obtained by sending a 1ms chirp pulse

The length of the pulse and the corresponding SNR's for both the short and chirp pulse should follow the relation:

$$\frac{\sqrt{\text{Duration of CHIRP pulse}}}{\sqrt{\text{Duration of short pulse}}} = \frac{\text{SNR of Chirp}}{\text{SNR of short pulse}} \quad (3.2)$$

The left hand side of equation 3.2 equals 22.3, while the right hand side equals 22.4. Hence this demonstrates that the improvement in SNR is directly proportional to the square root of the pulse length.

Figure 3.20 shows an image of J_{ab} obtained by scanning a 1 MHz transducer with a 2 μ s duration pulse on a thin gel phantom of a similar geometry as shown in figure 3.13. Figure 3.21 shows an image of J_{ab} obtained by scanning the same 1 MHz transducer with a 1 ms duration chirp having a frequency sweep of 0.7-1.3 MHz on the same thin gel phantom.

The image obtained by chirp has a much better SNR even with much less averaging i.e. 1/100th of the 2 μ s case.

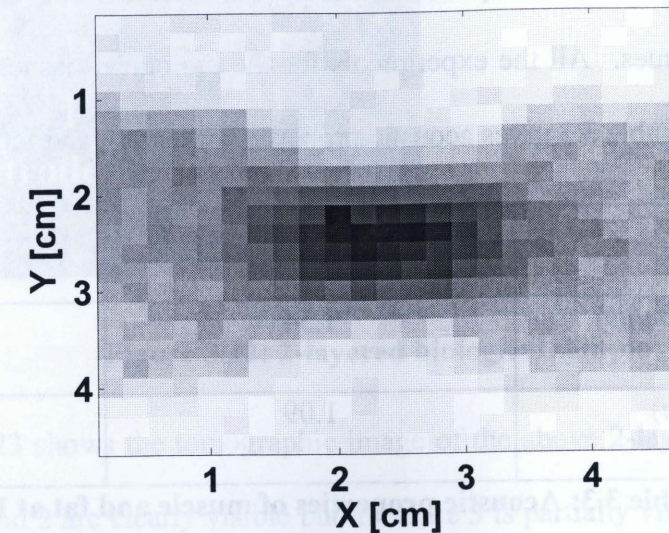


Figure 3.20: Image of J_{ab} by a short pulse of 2 μ s

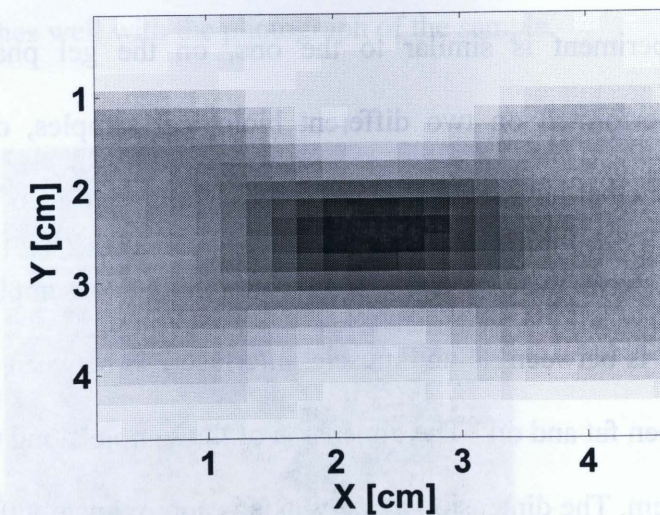


Figure 3.21: Image of J_{ab} by 1 ms chirp having a frequency sweep of 0.7-1.3 MHz

3.5 MAET images of biological tissues

After obtaining MAET signals from the gel phantoms, experiments are performed on biological tissues. For all the experiments fresh pork meat is used. The sample has layers of muscle and fat tissues. All the experiments for the biological tissues are performed with 1 MHz transducer. Table 3.3 gives acoustic properties of muscle and fat at 1 MHz [32].

	Muscle	Fat
Speed of Sound ($mm/\mu s$)	1.54	1.47
Attenuation (dB/cm)	1.09	0.48

Table 3.3: Acoustic properties of muscle and fat at 1 MHz

3.5.1 2D MAET images

2D MAET is used to obtain cross-sectional images in the x-y plane of thick biological tissues. This experiment is similar to the one, on the gel phantom in figure 3.10. Experiments are performed on two different biological samples, one having two layers (muscle-fat) and the other having four layers (muscle-fat-muscle-fat).

Figure 3.22 shows the top view of a 2-layered biological sample. Three interfaces are visible. Interface 1 is between oil and muscle, interface 2 is between muscle and fat and the interface 3 is between fat and oil. The dimension of the sample along the ultrasound z-axis is approximately 1.5 cm. The dimension along y-axis is approximately 0.9 cm. A pulse of 1 μs duration from a function generator is applied to the 1 MHz transducer. The scanning is done between the dashed lines along the x-axis with a step size of 2 mm.

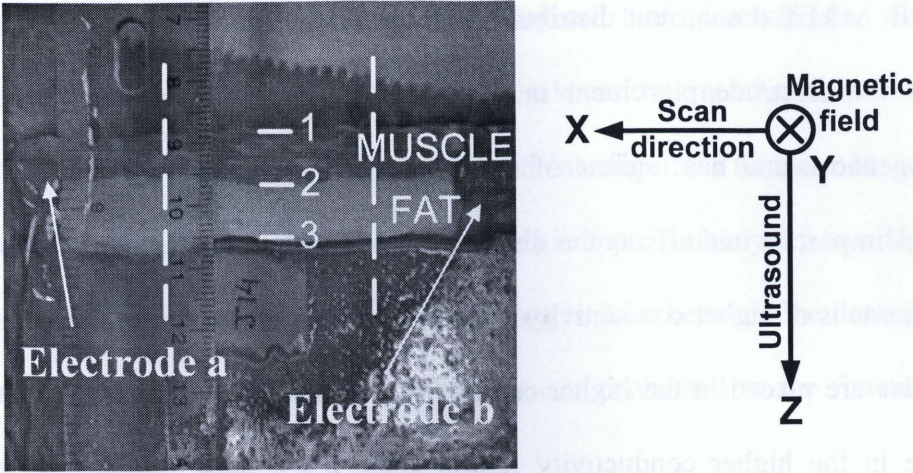


Figure 3.22: 2-layered biological sample

Figure 3.23 shows the tomographic image of the above 2-layered biological sample. The interface 1 and 2 are clearly visible but interface 3 is partially visible only near electrode 'b'. Some internal structures between interfaces 1 and 2 and interfaces 2 and 3 are also visible which cannot be seen with the naked eye. The cross-sectional geometry of the tomography matches well with the photograph of the sample.

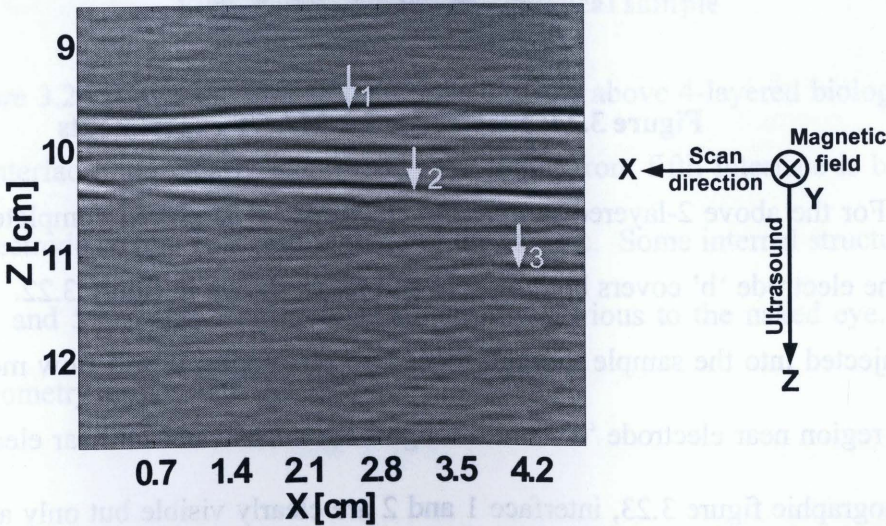


Figure 3.23: MAET tomography of a 2-layered biological sample

In MAET the current distribution is dependent upon the geometry of the sample as well as the electrode placement in the sample. Especially when the sample becomes inhomogeneous and has regions of varying conductivity then the placement of electrode becomes important and affects the distribution of current. For example if a sample has two regions, one is of higher conductivity while the other is of lower conductivity, and if both the electrodes are placed in the higher conductivity region, then the current distribution would only be in the higher conductivity region since it's a least resistive path. Now, if the electrodes are placed so that they cover both regions of conductivity, then the current will be distributed in both the regions with higher conductivity region having more current density than the lower conductivity region. The electrodes for MAET experiments are simply a bundle of small wires as shown in figure 3.24.

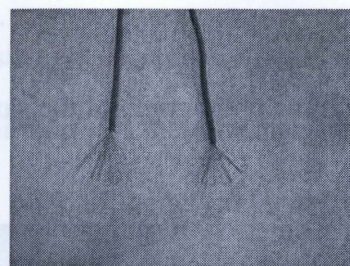


Figure 3.24: Electrodes for MAET experiments

For the above 2-layered sample the electrode 'a' is placed completely in the muscle while the electrode 'b' covers both muscle and fat as shown in figure 3.22. So if a current is to be injected into the sample through those two electrodes, it will flow mostly through the muscle region near electrode 'a', and through both muscle and fat near electrode 'b'. So in the tomographic figure 3.23, interface 1 and 2 are clearly visible but only a small portion of interface 3 which is near electrode 'b' is visible.

Figure 3.25 shows the top view of a 4-layered biological sample. Interface 1 is between oil and muscle, interface 2 is between muscle and fat, interface 3 between is fat and muscle, interface 4 is between muscle and fat and interface 5 is between fat and oil. The dimension of the sample along the ultrasound z-axis is approximately 3.5 cm. The dimension along y-axis is approximately 0.9 cm. The scanning is done between the dashed lines along x-axis with a step size of 1 mm. 1 MHz transducer connected to the function generator produces a 1 μ s acoustic pulse.

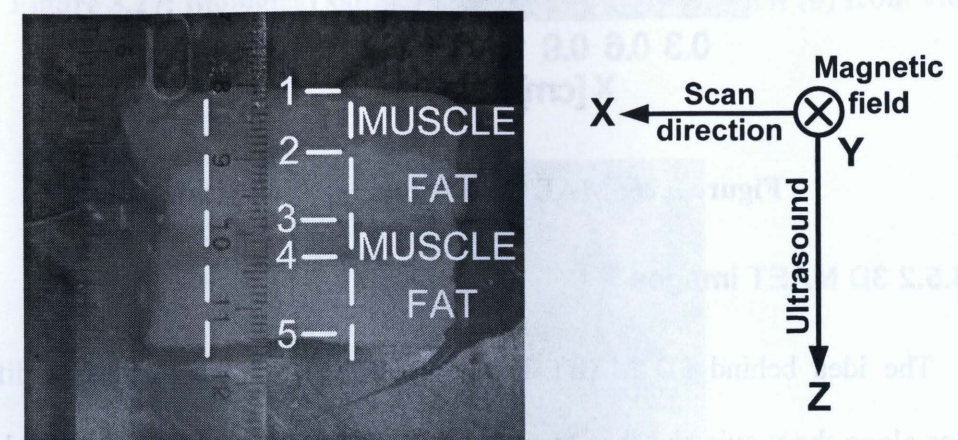


Figure 3.25: 4-layered biological sample

Figure 3.26 shows the tomographic image of the above 4-layered biological sample. First four interfaces are clearly identified. The signal from fifth interface is barely visible since the electrode covers first four regions of the sample. Some internal structures between interfaces 4 and 5 are also identified which are not obvious to the naked eye. The cross-sectional geometry agrees with the sample.

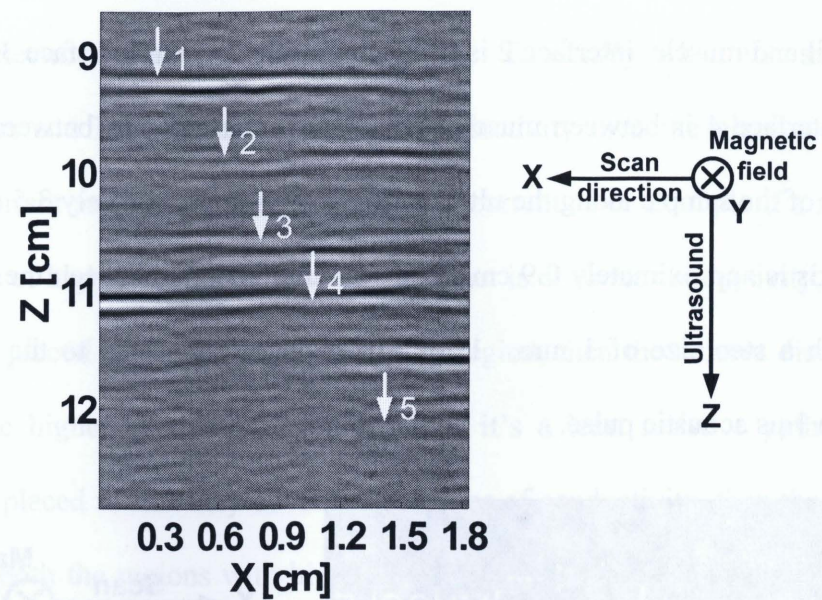


Figure 3.26: MAET of a 4-layered biological sample

3.5.2 3D MAET images

The idea behind 3D MAET is to obtain tomographic images at different cross-sections along the y-axis and then stack them in a sequence to obtain a complete 3D image data set. Figure 3.27 shows the top view and front view of the sample for 3D experiments. The sample is approximately 2 cm along z-axis and 0.9 cm along y-axis. It has three regions, muscle-fat-muscle. The front muscle region is clearly identifiable in the photo. The rear muscle is very thin, approximately 2 mm. In this experiment a high voltage pulser, which generates a negative 200 V pulse is connected to the 1 MHz transducer. The scanning step size along x-axis is 1 mm and along y-axis is 2 mm. The scanning region is identified by double ended arrows dashed lines for both x and y axes. The electrodes used in this experiment are shown in figure 3.28. The pins sticking out of the electrodes cover all the interfaces to improve the signal from each interface.

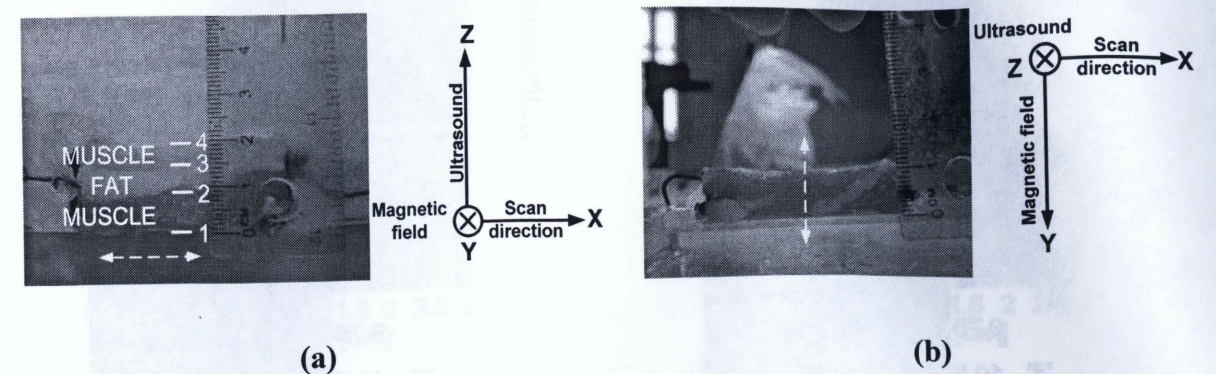


Figure 3.27: Biological sample for 3D MAET (a) top view (b) front view

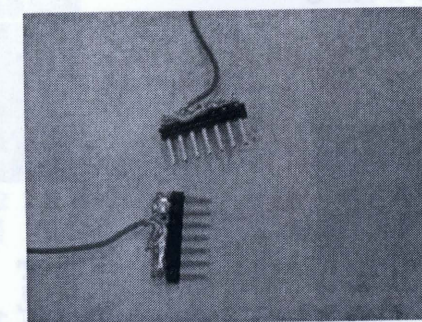
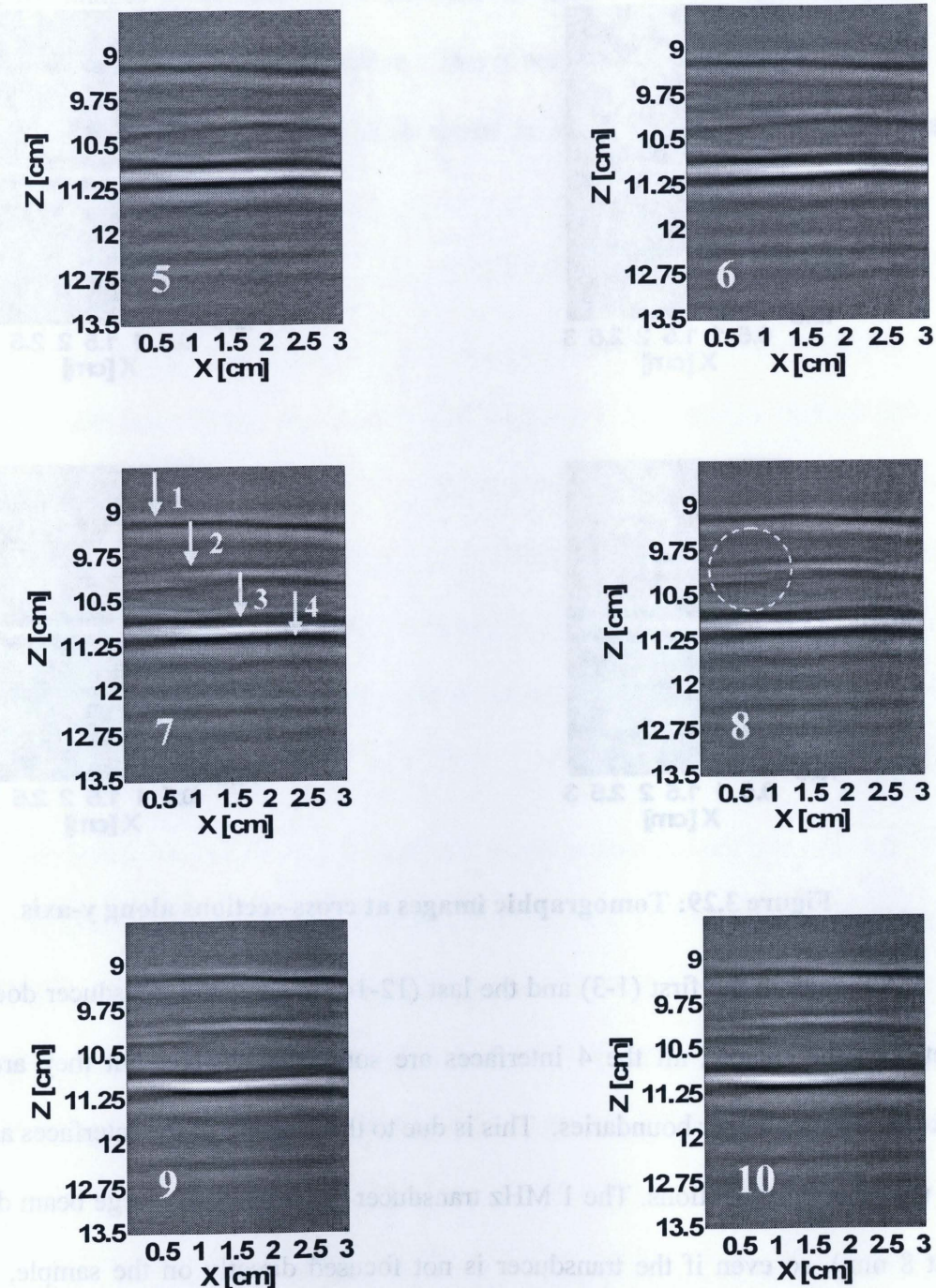
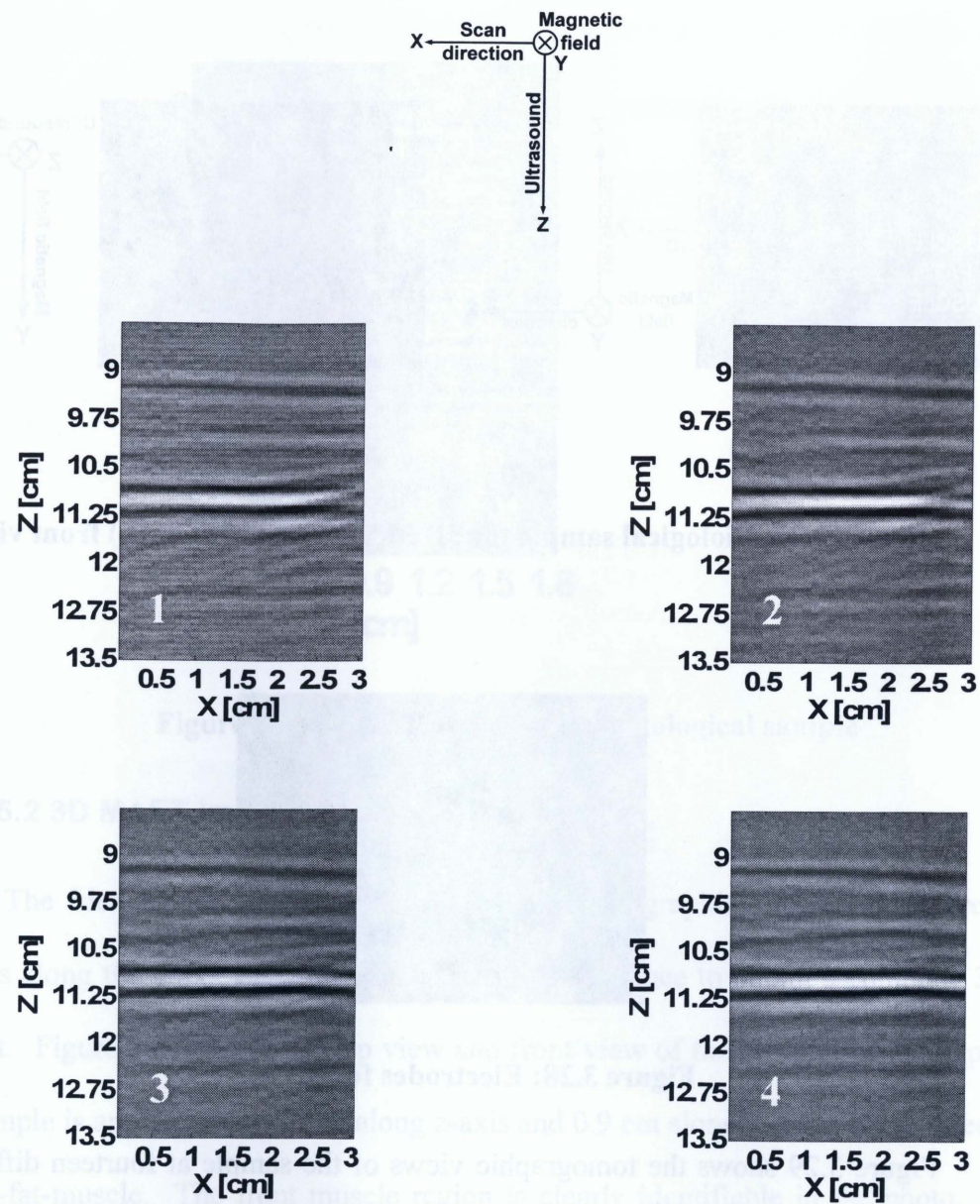


Figure 3.28: Electrodes for 3D MAET

Figure 3.29 shows the tomographic views of the sample at fourteen different cross-sections. All the four interfaces are clearly visible when the transducer is focused on the sample.



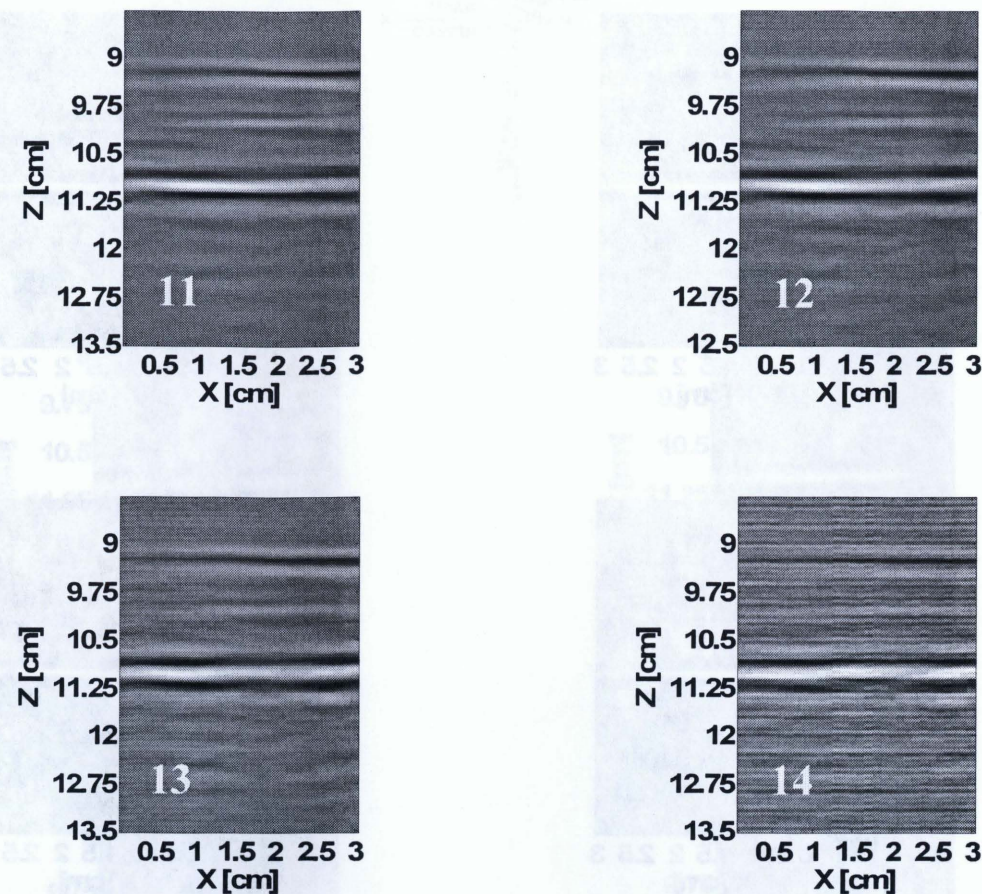


Figure 3.29: Tomographic images at cross-sections along y-axis

Although in the first (1-3) and the last (12-14) images, the transducer does not point directly on the sample, all the 4 interfaces are somewhat visible, but they are relatively weaker and have thicker boundaries. This is due to the blurring of the interfaces as compared with the other cross sections. The 1 MHz transducer has a relatively large beam diameter (of about 8 mm), so even if the transducer is not focused directly on the sample, part of the acoustic energy still falls on the sample and generates MAET signal. In image 7, all interfaces are clearly visible and have sharp boundaries because the focal point falls directly on the sample. When carefully observed differences in internal structures can also be found

among the images of different cross sections. In image 8, part of the interface 2 which is within the dashed circular line is broken. This is because the interface in the actual sample is curved at that point and in MAET a signal is weaker if the ultrasound does not fall perpendicularly on the sample face.

Chapter 4

Challenges and Conclusions

4.1 Challenges and possible solutions

I have presented a preliminary study on MAET as a potential imaging method for lead field current density and electrical impedance. High-spatial-resolution current density distribution is obtained for the first time for a thin gel phantom. Experimental results are compared with the numerical simulation and good agreement is observed. 2-D and 3-D MAET images for biological tissues are also obtained. But there are several challenges which need to be addressed before MAET can be a quantitative imaging modality of current density and electrical impedance.

The first and the foremost challenge is obtaining MAET signals from the interior of a homogeneous sample. So far the MAET signals are only detectable at the interfaces of two mediums of different conductivity. The signals from the interface are still useful and tell us about the electrical heterogeneity of the sample. But it is much more desirable to develop a quantitative imaging modality on electrical impedance by which signals can be obtained not only from the interfaces but also from the interior of the sample.

There are different ways which can be investigated to overcome the cancellation of the internal signals. One possible way is to use speckles that may occur when imaging biological tissues. In the ultrasound B-mode, the images of tissue contain a background that has a granular like appearance. It is due to the presence of many small randomly distributed

scatterers (such as those due to the cellular nature of tissue) and a coherent radiation source [32]. Therefore in sonography not only signals from the interfaces of the tissues are obtained but also the speckles from the interior homogeneous parts of the tissues. Similarly, small MAET signals are expected at the interfaces between cells and sub-cellular components. Many of these small signals add up together and this accumulation generates speckle, in the same manner as in sonography speckles are generated by many small, randomly distributed scattered acoustic waves. In sonography, speckles have been used to characterize the tissues [33-34]. In principle these methods can be adapted in MAET to analyze speckles in order to determine the local current density. Experiments discussed in this thesis are mostly performed by using 1 MHz transducer and no speckles are observed. Since the ratio between the signals generating speckles and the signals from interfaces increases with ultrasound frequency [35]. Therefore, in our future study we will use transducers with higher frequency to explore the speckles in MAET.

Another possible method to generate MAET signals from the homogeneous part of a sample is to utilize radiation force to generate non-linear MAET signals from the interior of samples by taking advantage of unidirectional nature of radiation force. When an acoustic wave is propagating in the medium, part of its energy is attenuated through absorption and scattering in the medium. Consequently, the momentum carried by the attenuated energy (or phonons) is transferred to the medium and a radiation force is exerted upon the medium. The radiation force can be static and dynamic. In the static case, the radiation force contains a static component pointing in the direction of wave propagation. Unlike the incident ultrasonic wave that oscillates in space, the radiation force does not. Therefore, the volume integral of the force and the induced motion in the medium will not be zero. Consequently,

the MAET signal in equation 2.8 generated by the static radiation force will not cancel out. Similar conclusions can be found out for dynamic radiation force if the frequency of radiation force is properly chosen. For example, if the dimension of the sample is 10 cm and the radiation force has a frequency of below 7.5 kHz, corresponding to a wavelength larger than 20 cm in soft tissues, the phase change in the whole 10 cm sample is smaller than π . Consequently, the MAET signal from different points of the interior of the sample will not cancel each other.

MAET signals are inversely proportional to the cross-sectional area of the sample under investigation. Normally the cross-sectional area of the subjects in clinical applications is much larger than that of the samples used in our initial experiments. Therefore, the MAET signals in clinical applications will be much weaker than these in our preliminary experiments. The strength of the signal can be improved by using a high voltage pulser to generate stronger ultrasound wave. Also the MAET signals are directly proportional to the strength of the magnetic field so a stronger magnet would improve the signal strength. Lastly, CHIRP can be used to improve the SNR of MAET signals further, as demonstrated in Chapter 3 of this thesis.

New methods need to be explored to detect the MAET signal. One possibility is to use coil as discussed in the end of chapter 2. This method is more robust than the detection by attaching electrodes to the sample. Because the detection with coil doesn't need the contact with the sample as in the electrode detection case, which might result in large variation in the detected signals due to the changes in electrode position and contact impedance between different measurements. In addition, the coil detection method provides

easier method for impedance reconstruction from the measurement of the lead field current density distribution [27].

4.2 Summary

This thesis presents a preliminary study on MAET as a potential imaging method for lead field current density and electrical impedance. Several experiments are performed on gel phantoms and excised biological tissues. MAET signal is verified for a thick gel sample by checking the flight time. High-spatial-resolution current density distribution is obtained for the first time for a thin gel phantom. Experimental results are compared with the numerical simulation and good agreement is observed. It is shown that chirp can be used to improve the SNR of MAET signals. 2-D and 3-D MAET images for biological tissues are obtained. Our investigations provide the proof-of-principle that MAET can be an imaging modality showing the interfaces between different biological tissues. But there are several challenges which need to be addressed before MAET can be a quantitative imaging modality of current density and electrical impedance. More investigations need to be carried out to understand the full potential of this novel imaging modality.

4.3 Conclusion

For thin samples high spatial resolution images for lead field current density distribution is obtained. For thick samples signals are only obtained from the interfaces that are related to the current density distribution. It is concluded that more rigorous investigations are required to make MAET a quantitative imaging modality.

Bibliography

- [1] <http://bibleprobe.com/humancell-lg.htm>.
- [2] F. S. Martinez, "Electrical Bio-impedance Cerebral Monitoring: Fundamental steps towards clinical application," PhD dissertation, Chalmers University of Technology, Göteborg, Sweden, 2007.
- [3] C. Polk and E. Postow, *The Handbook of Biological Effects of Electromagnetic fields*, CRC press, 1995.
- [4] K. R. Foster and H. P. Schwan, "Dielectric properties of tissues and biological materials - A critical review," *Critical Reviews in Biomedical Engineering*, vol. 17, pp. 25-104, 1989.
- [5] S. R. Smith, K. R. Foster and G. L. Wolf, "Dielectric properties of VX-2 carcinoma versus normal liver tissue," *IEEE Trans. Biomed. Eng.*, vol. 33, pp. 522-524, 1986.
- [6] K. J. Ellis, "Human body composition: In vivo methods," *Physiol. Rev.*, vol. 80, pp. 649-680, 2000.
- [7] J. Jossinet, "Variability of impedivity in normal and pathological breast tissue," *Med. Biol. Eng. Comput.*, vol. 34, pp. 346-350, 1996.
- [8] D. Holder, *Electrical impedance tomography: Methods, History, and Applications*, Bristol: Institute of Physics Publishing, 2005.
- [9] M. Cheney, D. Isaacson and J. C. Newell, "Electrical impedance tomography," *SIAM Rev.*, vol. 41, pp. 85-101, 1999.
- [10] J. Morucci and B. Rigaud, "Bioelectrical impedance techniques in medicines," *Crit. Rev. Biomed. Eng.*, vol. 24, pp. 467-597, 1996.
- [11] E. Demidenko, A. Hartov, K. Paulsen, "Statistical estimation of resistance/conductance by electrical impedance tomography measurements," *IEEE Trans. Med. Imag.*, vol. 23, pp. 829-838, 2004.
- [12] C. CohenBacrie, Y. Goussard, R. Guardo, "Regularized reconstruction in electrical impedance tomography using a variance uniformization constraint," *IEEE Trans. Med. Imag.*, vol. 16, pp. 562-571, 1997.
- [13] A. Adler, N. Shinozuka, Y. Berthiaume, R. Guardo, J. H. T. Bates, "Electrical impedance tomography can monitor dynamic hyperinflation in dogs," *J. Appl. Physiol.*, vol. 84, pp. 726-732, 1998.
- [14] A. Tidswell, A. Gibson, R. Bayford and D. Holder, "Validation of a 3D reconstruction algorithm for EIT of human brain function in a realistic head-shaped tank," *Physiol. Meas.*, vol. 22, pp. 177-185, 2001.
- [15] V. Kolehmainen *et al*, "Assessment of errors in static electrical impedance tomography with adjacent and trigonometric current patterns," *Physiol. Meas.*, vol. 18, pp. 289-303, 1997.
- [16] B. J. Roth, P. J. Basser, and J. P. Wikswo Jr., "A theoretical model for magneto-acoustic imaging of bioelectric currents," *IEEE Trans. Biomed. Eng.*, vol. 41, pp. 723-728, 1994.
- [17] H. Wen, "Volumetric hall effect tomography—a feasibility study," *Ultrason. Imag.*, vol. 21, pp. 186-200, 1999.
- [18] O. Kwon, E. Woo, J. Yoon, J. K. Seo, "Magnetic resonance electrical impedance tomography (MREIT) Simulation study of J-substitution algorithm," *IEEE Trans. Biomed. Eng.*, vol. 49, pp. 160-167, 2002.
- [19] R. Merwa, K. Hollaus, P. Brunner, and H. Scharfetter, "Solution of the inverse problem of magnetic induction tomography (MIT)," *Physiol. Meas.*, vol. 26, pp. S241-S250, 2005.
- [20] H. Griffiths, "Magnetic induction tomography," *Meas. Sci. Technol.*, vol. 12, pp. 1126-31, 2001.
- [21] H. Wen, "Feasibility of biomedical applications of Hall effect imaging," *Ultrason. Imaging*, vol. 22, pp. 123-136, 2000.

- [22] H. Wen, J. Shah and R.S. Balaban, "Hall effect imaging," *IEEE Trans. Biomed. Eng.*, vol. 45, pp. 119-124, 1998.
- [23] A. Montalibet, J. Jossinet and A. Matias, "Scanning electric conductivity gradients with ultrasonically induced lorentz force," *Ultrason. Imaging*, vol. 23, pp. 117-132, 2001.
- [24] A. Montalibet, J. Jossinet, A. Matias and D. Cathignol, "Electric current generated by ultrasonically induced Lorentz force in biological media," *Med. Biol. Eng. Comput.*, vol. 39, pp. 15-20, 2001.
- [25] S. Ballantine, "Reciprocity in electromagnetic, mechanical, acoustical and interconnected systems," *Proc. IRE*, vol. 17, pp. 929-951, 1929.
- [26] Y. Xu, S. Haider, A. Hrbek, "Magneto-Acousto-Electrical Tomography: A New Imaging Modality for Electrical Impedance," *13th International Conference on Electrical Bioimpedance combined with the 8th Conference on Electrical Impedance Tomography*, Graz (Austria), 2007.
- [27] S. Haider, A. Hrbek, Y. Xu, "Magneto-Acousto-Electrical Tomography: A Potential Method for Imaging Current Density and Electrical Impedance," *Physiol. Meas.*, vol. 29, pp. S41-S50, 2008.
- [28] J. Malmivuo and R. Plonsey, *Bioelectromagnetism - Principles and Applications of Bioelectric and Biomagnetic fields*, New York: Oxford University Press, 1995.
- [29] J. D. Jackson, *Classical Electrodynamics*, New York: Wiley, 1975.
- [30] M. O'Donnell, "Coded excitation system for improving the penetration of real time phased-array imaging systems," *IEEE Trans. Ultrason., Ferroelect., Freq. Contr.*, vol. 39(3), pp. 341-351, 1992.
- [31] R. Y. Chiao and X. H. Hao, "Coded excitation for diagnostic ultrasound: A system developer's perspective," *IEEE Trans. Ultrason., Ferroelect., Freq. Contr.*, vol. 52(2), pp. 160-170, 2005.

- [32] R. S. C. Cobbold, *Foundations of biomedical ultrasound*, New York: Wiley, 2007.
- [33] V. Dutt and J. F. Greenleaf, "Ultrasound echo envelope analysis using a homodyned k-distribution signal model," *Ultrason. Imag.*, vol. 16(4), pp. 265-287, 1994.
- [34] Y. M. Kadah, A. A. Farag, J. M. Zurada, A. M. Badawi and A. B. M. Youssef, "Classification algorithms for quantitative tissue characterization of diffuse liver disease from ultrasound images," *IEEE Trans. Biomed. Eng.*, vol. 15(4), pp. 466-478, 1996.
- [35] M. C. Kolios and G. J. Czarnota, "New insights into high frequency ultrasonic tissue scattering," *3rd International Symposium on Medical, Bio- and Nano- Electronics, Sensai (Japan)*, 2004.